Active phases for high temperature Fischer-Tropsch synthesis in the silica supported iron catalysts promoted with antimony and tin

Deizi Peron, Alan Barrios, Alan Taschin, Iulian Dugulan, Carlo Marini, Giulio Gorni, Simona Moldovan, Siddardha Koneti, Robert Wojcieszak, Joris Thybaut, et al.

March 6th, 2021

Active phases for high temperature Fischer-Tropsch synthesis in the silica supported iron catalysts promoted with antimony and tin

Deizi V. Peron[a], Alan J. Barrios[a, b], Alan Taschin[a], Iulian Dugulan[c], Carlo Marini[d], Giulio Gorni[d], Simona Moldovan[e], Siddardha Koneti[e], Robert Wojcieszak[a], Joris W. Thybaut[b], Mirella Virginie[a] and Andrei Y. Khodakov[a]*

[a]*Univ. Lille, CNRS, Centrale Lille, Univ. Artois, UMR 8181 – UCCS – Unité de Catalyse et Chimie du Solide, F-59000 Lille, France*

[b]*Laboratory for Chemical Technology (LCT), Department of Materials, Textiles and Chemical Engineering, Ghent University, Technologiepark 125, 9052 Ghent, Belgium*

[c]*Fundamental Aspects of Materials and Energy Group, Delft University of Technology, Mekelweg 15, Delft, 2629 JB, Netherlands*

[d]*ALBA Synchrotron Light Source, Crta. BP 1413, Km. 3.3, 08290 Cerdanyola Del Vallès, Barcelona, Spain*

[e]*Groupe de Physique des Matériaux, CNRS, Université Normandie & INSA Rouen Avenue de l'Université - BP12, 76801 St Etienne du Rouvray, Francee*

Abstract

Fischer-Tropsch synthesis provides an important opportunity for utilization of biomass and plastic waste. Iron catalysts are the catalysts of choice for light olefin synthesis using Fischer-Tropsch reaction. In this paper, we investigate strong promoting effects of antimony and tin on the catalytic performance of silica supported iron Fischer-Tropsch catalysts using a combination of advanced and *in-situ* techniques. The catalyst doping with these elements added *via* impregnation results in a major increase in the reaction rate and much better catalyst stability. No enhancement of iron dispersion was observed after the promotion, while somewhat higher extent of iron carbidization was observed in the antimony promoted catalysts. Iron-bismuth bimetallic nanoparticles are detected by several techniques. In the working catalysts, the promoters are located in close proximity to the iron nanoparticles. The promotion leads to the 7-10 times increase in the intrinsic activity of iron surface sites due to their interaction with the promoters.

Keywords: biomass; syngas; Fischer-Tropsch; iron; promotion

Introduction

Fischer-Tropsch (FT) synthesis is an attractive way to convert syngas generated from non-petroleum and renewable feedstocks such as biomass, plastic and organic waste into fuels and chemicals. Iron catalysts are the catalysts of choice [1,2] for high temperature FT synthesis, which can produce a larger fraction of olefins. Activity, selectivity to light olefins and catalyst stability are major challenges of FT synthesis over iron catalysts. FT synthesis is a complex reaction. The reaction rate and selectivity to the target hydrocarbons depend on the rate of different elementary steps. The selectivity of FT synthesis is usually following a rather broad Anderson-Schulz Flory distribution.

FT synthesis on iron catalysts involves iron carbide phases [3]. Both bulk and supported iron catalysts have been used for high temperature FT synthesis. Commercial iron FT catalysts are unsupported, fused or precipitated catalysts promoted with copper or manganese, potassium, and silica [4–6]. The advantages of the supported iron catalysts are related to higher dispersion of active phase and potentially better mechanical stability. Preparation of iron catalysts for FT synthesis is a complex process [4] intended to result in the materials with desirable chemical, physical, catalytic and mechanical properties. The supported iron catalysts are usually prepared by impregnation followed by drying, calcination and activation in carbon monoxide or syngas.

Promotion is one of the common approaches to improve the performance of iron catalysts. Two types of promoters [7]: electronic promoters and structural promoters, are usually considered for enhancement of the FT catalytic performance. The electronic promoters [8] enhance the intrinsic activity of the active sites. They can affect the intrinsic rate of the reaction elementary steps and shift the reaction selectivity to the target products, while the structural promoters[9] increase the dispersion of active phase, stabilize the catalyst surface and improve the mechanical strength. The overall enhancement of the catalytic performance

on the promotion is often an interplay [7] of the electronic and structural promoters, their concentration, coverage and interaction with the active phase.

Alkali metals [3,10–15] and copper [10,15,16] have been traditionally used as promoters for iron FT catalysts. Alkali promoters affect the electronic state of iron and support. They usually decrease the methane selectivity and shift the hydrocarbon distribution to long chain hydrocarbons, while copper enhances iron reducibility and carbidization. Much higher reaction rates have been often observed [17] on copper-promoted iron catalysts than on the potassium-promoted and unpromoted counterparts, while the promotion with potassium had a stronger impact on the selectivity. The group of de Jong [18–20] has proposed simultaneous promotion with sodium and sulfur for the enhancement of synthesis of light olefins over iron catalysts. They suggested [21] that sulfur could shift the selectivity toward the short-chain C_2–C_4 hydrocarbons without a simultaneous increase in the selectivity to methane, while the presence of alkali ions increased the olefin to paraffin ratio.

Our recent study [22] addressed screening 29 elements, as promoters for silica supported iron Fischer-Tropsch catalysts using a high throughput experimentation (HTE) approach. We found [22–24] that the performance of iron catalysts could be enhanced by promotion with soldering metals. The promotion of iron catalysts with bismuth and lead resulted in a remarkable increase in the carbon monoxide hydrogenation rate, light olefin selectivity and productivity with a possibility to conduct Fischer–Tropsch synthesis at low reaction pressure. In previous reports [22–26], we showed that bismuth and lead showed the properties of both electronic and structural promoters. The bismuth and lead promoted catalysts exhibited 2-3 times higher intrinsic activity [25] (TOF) relative to the non-promoted iron catalyst with the 60% increase in the selectivity to light olefins. The catalyst stability against sintering and carbon deposition was also enhanced in the presence of bismuth. A detailed *in-situ* characterization study [26] uncovered a remarkable mobility and versatility of bismuth under

the reaction conditions. Bismuth metallic species, which transform into larger spherical bismuth liquid droplets under the reaction temperatures readily migrate over the catalyst surface, with the formation of iron-bismuth core–shell structures. In the working FT catalysts, metallic bismuth located at the interface of iron species undergoes continuous oxidation and reduction cycles [26], which facilitate carbon monoxide dissociation.

HTE experiments [22] showed that the promotion of iron catalysts with tin and antimony also led to a major increase in the FT reaction rate [22]. Both tin and antimony have relatively low melting temperatures. Their Tammann and Hüttig temperatures [27], corresponding respectively to bulk and surface mobilities are well below the reaction temperature of high temperature FT synthesis. This suggests that these promoters can be also mobile under the reaction conditions. At the same time, very few information is available about the active species, which form on addition of tin and antimony to iron catalysts and their role in FT synthesis.

The goal of this work is to elucidate the genesis and evolution of active phases in the silica supported iron catalysts promoted with antimony and tin during their activation and catalytic reaction using a combination of *in-situ* and advanced characterization techniques. The characterization results are discussed alongside with the catalytic results obtained in a high-pressure catalytic reactor.

Experimental

Catalyst preparation

The catalysts were prepared using commercial amorphous silica (CARIACT Q-10, Fuji Silesia) as a support. Two types of catalyst preparation procedures were used: impregnation and mechanical mixing. The $FeSn/SiO_2$ catalyst was prepared by co-impregnation using aqueous solutions of tin (II) chloride ($SnCl_2$, Sigma-Aldrich) and iron nitrate

($Fe(NO_3)_3.9H_2O$, Sigma-Aldrich). For the synthesis of $FeSb/SiO_2$, silica was impregnated first with antimony (III) chloride ($SbCl_3$, Sigma-Aldrich) and then with iron nitrate ($Fe(NO_3)_3.9H_2O$, Sigma-Aldrich). The non-promoted $Fe(20\%)/SiO_2$ catalyst prepared by impregnation with iron nitrate was used for mechanical mixing. After the impregnation, the samples were dried in oven at 100 ºC for 12 h followed by calcination in air at 400 ºC for 6 h with the heating ramp of 1 ºC/min. The $FeSb/SiO_2$ (m) and $FeSn/SiO_2$ (m) samples were prepared by mechanical mixing of $Fe(20\%)/SiO_2$ and Sb/SiO_2, $Fe(20\%)/SiO_2$ and Sn/SiO_2 catalysts, respectively. The Fe content in the final catalysts prepared by impregnation and mechanical mixing was fixed at 10 wt. %, while the molar ratios of Fe/Sb and Fe/Sn were 100:2.

Catalyst characterization

The N_2 physisorption measurements were performed on a Micromeritics Tristar II PLUS Surface Area and Porosimetry analyzer. The samples were degassed under vacuum at 250 ºC for 2 h. The nitrogen adsorption-desorption isotherms were measured at -196 ºC. The specific surface area of the samples was calculated by the BET method.

The chemical composition of the samples was determined by X-ray fluorescence (XRF) using a M4 TORNADO (Bruker) spectrometer. The instrument was equipped with 2 anodes, a rhodium X-ray tube (50 kV/600 mA, 30 W), tungsten X-Ray tube (50 kV/700 mA, 35 W) and a Silicon-Drift-Detector (<145 eV resolution at 100000 cps (Mn Kα) with a Peltier cooling to 253 ºC). To characterize the samples, the rhodium X-rays with a poly-capillary lens enabling excitation of an area of 200 µm were used and the measurements were conducted under vacuum (20 mbar). Quantitative analysis was performed using fundamental parameter (FP, standardless).

The reduction behavior of the catalysts was examined by hydrogen temperature-programmed reduction (TPR) using an AutoChem II 2920 apparatus (Micromeritics). The samples (0.05 g) were reduced in a flow of 5% H_2/Ar flow (30 mL/min) and heated up to 1100 ºC with the temperature ramp rate of 10 ºC/min.

The samples were characterized by X-ray powder diffraction (XRD) using a Bruker AXS D8 diffractometer with a monochromatic Cu Kα radiation (λ =0.1538 nm). The XRD patterns were collected with the 2θ range between 20 to 70°, using a step size of 0.02° and with an acquisition time of 0.5 s. The identification of the phases present in the catalysts was carried out by comparison with the JCPDF standard spectra software.

To determine the carbon deposition in the catalysts, the thermogravimetric analysis was performed using a SDT Q600 V20.9 Build 20 Thermogravimetric Analyzer (TGA) & Differential Scanning Calorimeter (DSC) with the 10 mg sample, submitted to a temperature ramp of 5 ºC/min until 600 ºC under air.

The transmission ^{57}Fe Mössbauer spectra were collected at -153 °C or room temperature with a sinusoidal velocity spectrometer using a ^{57}Co(Rh) source. The velocity calibration was carried out using an α-Fe foil at room temperature. The source and absorbing samples were kept at the same temperature during the measurements. The Mössbauer spectra were fitted using the Mosswinn 4.0 program [28]. The *in-situ* experiments were performed at the pressures up to 10 bar, in a state-of-the-art high-pressure Mössbauer *in-situ* cell – recently developed at the Reactor Institute in Delft [29]. The high-pressure beryllium windows used in this cell contain 0.08 % Fe impurity whose spectral contribution was fitted and removed from the final spectra.

The X-Ray Photoelectron Spectra (XPS) were obtained using a Kratos AXIS UltraDLD spectrometer working with Al Kα X-rays at 1486.7 eV. The XPS spectra of the fresh catalyst were first measured and then the catalyst was placed into the *in-situ* reaction cell heated under

a flow of CO (50 mL/min, 1 bar) from room temperature up to 250 ºC and after 350 °C at a heating rate of 5 °C/min and kept for 1 h at each temperature.

The Scanning Transmission Electron Microscopy (STEM) analyses were carried on a double corrected analytical TEM 200 CF operating at 200 kV. Elemental mapping of the elements of interest (256 x 256 px) was carried out using the Energy Dispersive X-ray Spectrometer (EDX) Centurio 100 detector with a scanning speed of 0.05 msec/px, whilst applying a drift correction every 60 seconds. STEM micrographs were acquired using a High Angular Annular Dark Field (HAADF) detector and a camera length of 8 cm, with a spot diameter of 0.1 nm.

The *in-situ* Sb K-edge and Sn K-edge X-ray absorption spectroscopy (XAS) spectra were measured at Beamline CLÆSS of the ALBA synchrotron (Barcelona, Spain). The X-ray energy range 2.4 - 63.2 keV can be covered, using pairs of Si(111) and Si(311) crystals. The current signals from the ionization chambers were collected, amplified and converted to output voltage by the ALBA Electrometer. For the *in-situ* XANES and EXAFS measurements, the sample was pressed into a pellet with a 5 mm diameter and added in a reactor ITQ-ALBA Multipurpose Cell (**Figure S1, Supplementary Material (SM)**) [30]. The measurements were performed in presence of CO (P=1 bar) for cabidization and syngas (H_2/CO=1, P=7 bar) for the FT reaction at temperature ranging from ambient to 350 ºC. The data were collected in transmission mode and analyzed with the Athena software [31].

Catalytic tests

The catalytic performance of SiO_2-supported iron catalysts was measured using reactors with the internal diameter of 2 mm, where 100 mg of fresh catalyst have been loaded into the reactor. The catalyst was activated with a heating ramp of 2 ºC/min until reaching the temperature of 350 ºC and dwelling at that temperature for 10 h under CO flow ($4.1x10^{-}$

^{4} mol/min) at atmospheric pressure. After cooling down to 180 ºC, syngas with H_2/CO = 1/1 was introduced into the reactor. Nitrogen with flow of 1 cm^3/min was used as internal standard for the calculation of CO conversion. After the flow rates and pressure have been stabilized, the temperature was increased up to 350 ºC to start the reaction. For the analysis of the reagents and reaction products, a Varian CP-3800 chromatograph equipped with a thermal conductivity detector (TCD) and a flame ionization detector (FID) was used. Two columns were used for this analysis, the first is a packed CTR-1 column connected to the TCD, and the second is a Rt-Q-PLOT capillary column connected to the FID.

The TOF values were obtained as proposed by de Jong [32] et al. using the density of Hägg iron carbide Fe_5C_2 (ρ = 7.57 g/cm^3) and assuming 14 Fe atoms/nm^2. Also, it has been assumed that the spherical iron-containing particles consist completely of iron carbide at their surfaces. The number of surface iron carbide sites was calculated from the particle size measured by the TEM analysis.

Results

Ex-situ characterization

The XRF elemental analysis data for the Sn and Sb promoted catalysts (prepared by impregnation and mechanical mixture) are displayed in **Table 1**. All the catalysts have iron contents similar to the inventory (around 10 wt. %) in most of samples and 21 wt. % in Fe(20%)/SiO_2. The Sn and Sb promoter contents were close to 0.7 - 0.8 wt. %. The XRD patterns of the Fe/SiO_2 reference iron catalyst and those impregnated with the Sn and Sb promoters are available from our previous report[22]. **Figure 1a** shows the XRD patterns of the Fe/SiO_2 (20%) catalyst and those prepared by mechanical mixture of Fe(20%)/SiO_2 and Sn/SiO_2 or Sb/SiO_2. The calcined catalysts display distinguished diffraction peaks of the hematite phase (Fe_2O_3, JCPDS13-0534). No diffraction peaks attributed to the crystalline

phases of the antimony and tin promoters were observed. The Scherrer equation has supplied additional information about the iron oxide crystallite size (**Table 1**). Note that $Fe/SiO_2(20\%)$ has slightly larger iron oxide crystallites compared to Fe/SiO_2 with the iron content of about 10 wt.%. As expected, the addition of Sn and Sb promoters by mechanical mixing to the $Fe/SiO_2(20\%)$ catalyst seems to have no effect on the iron oxide dispersion, the hematite crystallites sizes measured by XRD were around 20 nm, which is essentially the same as on relevant silica supported iron catalyst. In the $FeSn/SiO_2$ catalysts prepared by co-impregnation, the hematite crystallite sizes were slightly smaller compared to the reference Fe/SiO_2 catalyst [22].

We also performed XRD measurements (**Figure 1b**) for the non-promoted and promoted iron catalysts (prepared by mechanical mixing) after FT reaction. The diffraction peaks at the 2θ angle of about 44° for all the catalysts are attributed to the iron carbide phases. For this study, the width of the iron carbide XRD peak was not much affected by the promoters. Our previous magnetization data [33] suggest that χ-Fe_5C_2 or ε-Fe_2C can contribute to the intensity and width of the XRD peak at 2θ angle of 44°. This suggests that the unambiguous identification of specific iron carbide phases could be difficult from the XRD patterns. The apparent sizes of iron carbide nanoparticles calculated from the XRD peaks for these catalysts using the Scherrer equation were around 5 nm. These sizes are underestimated due to the possible overlapping of several XRD peaks of iron carbide phases.

Figures 2 - 4 show the STEM-HAADF (High Angle Annular Dark Field) micrographs and STEM-EDX (Energy Dispersive X-ray Spectroscopy) elemental maps for the fresh Fe/SiO_2, $FeSn/SiO_2$ and $FeSb/SiO_2$ impregnated catalysts and those after activation in CO. Two types of support morphologies are identified in Fe/SiO_2 (**Figure 2a**): porous support constituted by small grains with sizes <20 nm and heterogeneous support formed by the co-existence of large grains (sizes >50nm, blue arrows) with small grains disposed in a porous non-regular

matrix. Owing to the Z contrast achieved in the STEM-HAADF imaging mode, the presence of high Z elements such as Fe, is unambiguously determined (**Figure 2a**). The Fe particles are uniformly distributed on/within the porous support (white features in the STEM-HAADF micrograph). The Fe particle sizes range from 10 nm to 100 nm. In the calcined $FeSn/SiO_2$ catalyst (**Figure 3a**), the Fe nanoparticles are also uniformly dispersed on the SiO_2 porous support with the size slightly larger than for Fe/SiO_2. STEM-EDX confirms the presence of Sn homogenously distributed within the specimen. In calcined $FeSb/SiO_2$ (**Figure 4a**) catalyst, we also detected a homogenous distribution of Fe nanoparticles with the sizes <100 nm on the porous support constituted by the SiO_2 grains. Antimony was also homogeneously distributed over SiO_2. The Sb quantification was not possible however, from EDX, because the Sb peak is superimposed with the Si K line.

In order to get deeper understanding on the catalyst evolution prior to the reaction, the STEM-EDX analysis was also conducted for the activated iron catalysts. In the activated Fe/SiO_2 catalyst (**Figure 2b**), both individual small Fe nanoparticles and larger agglomerates of about 100 nm were detected. The activated $FeSn/SiO_2$ catalyst (**Figure 3b**) shows the regions of the specimens with different sizes, shapes and morphologies of the support and/or nanoparticles. The size of Fe nanoparticles varies between 20 and 100 nm and their shapes varies from rounded to platelets. No Sn-containing nanoparticles area is observed and the Sn seems highly dispersed on the silica support. A careful analysis of the high-resolution STEM-HAADF images however, identified the presence of the tin atoms and atomic clusters in the close proximity of the iron nanoparticles (**Figure S2, SM**).

The activated $FeSb/SiO_2$ catalyst (**Figure 4b**) displays iron nanoparticles with sizes comprised between 10 and 50 nm and larger nanoparticle agglomerates. The nanoparticles show a core-shell morphology, with the core rich in Sb and the shell constituted mainly by iron. The Fe shell appears to be oxidized probably due to the exposure of the activated

nanoparticle to air and catalyst surface passivation**. Figure 5** displays the histogram of iron nanoparticle distribution calculated from the STEM images of the activated catalysts using at least 50 iron nanoparticles. The average iron nanoparticle size is of 14.2 nm in the activated Fe/SiO_2 catalyst (**Figure 5a**), while the promotion results in the increase in the iron nanoparticle size to 26.7 nm for $FeSn/SiO_2$ (**Figure 5b**) and 29.0 nm for $FeSb/SiO_2$ (**Figure 5c**).

Reducibility is an important feature of iron catalysts. **Figure 6** shows the H_2-TPR profiles for iron catalysts promoted with Sn and Sb via mechanical mixing. The H_2-TPR profiles of the catalyst prepared by impregnation are available in our previous report [22]. The hydrogen consumption amounts measured by TPR principally provide therefore, useful information about the iron reduction. The TPR profiles display three main hydrogen consumption peaks, which are attributed to the step-wise iron reduction from hematite to metallic iron:

$$Fe_2O_3 \rightarrow Fe_3O_4 \rightarrow FeO \rightarrow Fe$$

The TPR profiles are consistent with previous works [34–37], the first peak at 340-420 ºC is generally related to the reduction of hematite (Fe_2O_3) to magnetite (Fe_3O_4), the second peak can be associated with the reduction of magnetite (Fe_3O_4) to wüstite (FeO), while the third peak at 650-700ºC can be attributed to the last step of iron reduction from wüstite (FeO) to metallic iron (Fe). Also, we observe an intense peak at temperatures exceeding 1000 °C that can be linked to hardly reducible iron silicate species. The promotion with Sb and Sn slightly affects the position of TPR peaks for iron catalysts. In order to determine the peak temperatures with a better accuracy, the TPR profiles were deconvoluted (**Figure S3, SM**). Almost all TPR peaks slightly shift to lower temperatures on the promotion with antimony and tin (**Figure 6**), while the first peak referring to the reduction of hematite to magnetite slightly shifts to higher temperature (from 365 ºC to 390 ºC). At the same time, the overall

hydrogen consumptions are similar on the non-promoted iron catalyst and the counterparts promoted with Sb or Sn (**Table 1**).

Figures 7 and **S4, SM** show the thermogravimetric analysis (TGA) results of activated and spent catalysts prepared respectively by impregnation and mechanical mixing, under an air atmosphere. The thermograms show a first weight loss between 80 °C to 150 °C, that can be associated to physisorbed water removal and dehydration of iron oxyhydroxide (FeOOH) generated by ambient moisture. Furthermore, the significant weight losses within 350-550 °C can be assigned to the combustion of carbonaceous deposits. This loss is smaller for the catalysts activated in CO (**Figure 7a** and **S4a, SM**). It corresponds to the combustion of iron carbides in the activated samples. Interestingly, the weight loss was more significant for the antimony and tin promoted catalysts prepared by impregnation than for the non-promoted Fe/SiO_2. This can be attributed to higher extent of iron carbidization. Note that mechanical mixing of the promoters and iron catalysts does not result in a more important weight loss after the catalyst activation in CO compared to the non-promoted iron catalyst (**Figure S4a, SM**). It seems that mechanical mixing does not much affect iron carbidization. The TGA results are consistent with the Mossbauer data, which are presented and discussed below.

The weight loss is more significant for the catalysts, which were exposed to FT reaction (**Figure 7b** and **S4b, SM**). For the spent catalysts, the higher loss corresponds to the oxidation of carbon species, which may have been deposited on the catalysts during the FT reaction. It can be clearly seen that the Sn and Sb promoters inhibit carbon deposition on catalyst surface. The spent Sn- and Sb-promoted catalysts prepared by impregnation show ~60 % and 30 % smaller deposition respectively compared to the reference non-promoted Fe/SiO_2 catalyst. This smaller amount of carbon deposition seems to contribute to better stability of the Sn- and Sb-promoted catalysts in FT reaction. In our previous work [38], the carbon deposition was reduced in the iron catalysts promoted by bismuth. The observed phenomenon was explained

by the continuous carbon removal from the surface by mobile promoter. A similar mechanism can possibly operate for antimony.

Since the catalytic processes occur on the surface, the surface structure of iron catalysts was studied by XPS (**Figure 8**). The Fe 2p XPS spectra (**Figure 8a** and **8b**) for calcined catalysts display peaks at ~711.2 eV (Fe $2p_{3/2}$) and ~724.3 eV (Fe $2p_{1/2}$) with a shakeup satellite structure at ~719.2 eV. The shape of the peaks combined with the binding energies clearly indicate the presence of Fe^{3+} species. The XPS data are consistent with XRD that showed the presence of (Fe_2O_3) hematite phase in the calcined catalysts. After treatment with CO at 350 °C, the XPS spectra present noticeable changes. First, the peaks assigned to Fe^{3+} in $FeSb/SiO_2$ considerably decrease in intensity. The ratio of the I_{Fe}/I_{Si} XPS signals decreases from 0.527 to 0.344, which can be attributed to iron sintering (**Table 2**). Also, a shoulder appears at around 710 eV, which can be attributed to iron carbide [25,26,39]. This confirms the presence of iron oxide and iron carbide in the activated catalysts. In addition, after the CO treatment, another peak appears at ~716.5 eV in the XPS spectrum of activated $FeSn/SiO_2$, that can be assigned to the Sn $3p_{3/2}$ level. The Sn $3p_{3/2}$ peaks at 716.5 eV can be attributed either to the Sn^{4+} or Sn^{2+} species. The major increase in the intensity of this peak after the treatment with CO suggests an increase in the surface Sn concentration and tin redispersion on the catalyst surface.

The Sb 4d XPS spectra are shown in **Figure 8c**. The presence of a broad peak ~35 eV demonstrates the presence of oxidized Sb. The deconvolution of this peak generates two peaks at ~35.9 eV and ~34.7 that can be assigned respectively to the Sb $4d_{5/2}$ and $4d_{3/2}$ components in the Sb_2O_3. Note that XPS did not detect any noticeable concentration of Sb_2O_5 in the calcined $FeSb/SiO_2$ catalyst (Sb 4d binding energies of 36.70 and 35.50 eV in Sb_2O_5). The broad low-intense feature at 25 eV can be assigned to the O 2s peak. The treatment in CO leads to partial Sb reduction to metallic state with a characteristic XPS peak at ~32.3 eV. The

Sb/Si XPS ratio does not change after the catalyst activation in CO (**Table 2**). This suggests that no visible changes in the Sb dispersion, which might occur during the activation. These data are further corroborated with the XAS experiments presented below. The Sn 3d XPS spectra are shown in **Figure 8d**. The calcined catalyst exhibits XPS peaks with the binding energies of 486.2 and 494.6 eV that are assignable[40] to Sn $3d_{5/2}$ and Sn $3d_{3/2}$ and that are characteristics of the Sn^{2+} species. After the CO treatment, a displacement of the Sn 3d XPS signal to higher binding energies is observed. The peak at 487.5 eV can be related to the framework Sn^{4+} species in the materials, in which Sn^{4+} substituted the Si^{4+} atoms as previously stated by Pachamuthu [41] et al. Also, the increase in the I_{Sn}/I_{Si} XPS ratio from 0.123 to 0.431 (**Table 2**) confirms tin redispersion on the catalyst surface at high temperature in CO. This suggestion is consistent with the increase in the intensity of the Sn $3p_{3/2}$ peak at 716.5 eV (**Figure 7b**) observed after the exposure to CO.

In-situ Mossbauer measurements

To identify different Fe species and correlate them with the catalytic performance, we performed *in-situ* Mössbauer spectrometric investigation of the non-promoted Fe/SiO_2, Sb- and Sn-promoted catalysts prepared by impregnation and mixing under CO and syngas. The Mössbauer spectra were measured at -153 °C (**Figures 9** and **10**) and at room temperature (**Figures S5** and **S6, SM**). **Table 3** displays the Mössbauer fit parameters of fresh catalysts and catalysts exposed to syngas *in-situ* under the conditions similar to those in the catalytic tests. The Mössbauer fit parameters of the catalysts activated in CO are given in **Table S1, SM**. Analysis of all fresh catalysts reveals the presence of hematite species (Fe_2O_3). This observation agrees well with the XRD and XPS data. Then, the catalysts were *in-situ* activated in CO at 350°C at 1 bar and then exposed to syngas under the FT reaction

conditions (H_2/CO=1, P=10 bar). The Mossbauer spectra of the spent catalysts were measured at -153°C without exposure of the catalysts to air (**Figure 10**).

The Mössbauer spectra of the activated and spent catalysts are rather different from the fresh ones. Iron species are present in the spent Fe/SiO_2 catalyst as 70% Hägg carbide and 30% wüstite (**Table 3**). An obvious promoting effect is observed for the FeSb/SiO_2 sample, in which the fraction of Hägg carbide increases to ~90%. The promotion with Sb seems to enhance iron carbidization. In the FeSn/SiO_2 sample, the extent of carbidization is lower and the fraction of wüstite is higher ~57%. The fraction of the Hägg carbide formed after the FT reaction with the Fe(20%)/SiO_2 sample is ~76%, which is higher than in the non-promoted Fe(10%)/SiO_2 catalyst (70%), but lower than in the Sb-promoted catalyst (78-80%). Higher extent of carbidization in Fe(20%)/SiO_2 compared to Fe/SiO_2 can be due to larger iron particle sizes (**Table 1**). Indeed, previously it was shown [33] that larger iron oxide particles are easier to carbidize than smaller ones.

In-situ XAS characterization of the Sn and Sb promoters

The *in-situ* XANES spectra at the Sb K- and Sn K-absorption edges in the iron catalysts prepared by impregnation and mechanical mixing and their evolution during the catalyst activation in CO are shown in **Figures 11.** The comparison with the reference spectra [42] suggests that in the calcined FeSb/SiO_2 catalyst, antimony is present as Sb_2O_5. The FeSb/SiO_2 (m) catalyst prepared by mechanical mixing in addition to Sb_2O_5 also contains about 20% of Sb_2O_3. Exposure of the antimony-promoted catalysts to CO during temperature ramping results in gradual evolution of the XANES spectra (**Figure 11 a and b**). Analysis of the XANES data suggests that the reduction of Sb_2O_5 species to metallic state in the CO flow proceeds *via* intermediate formation of Sb_2O_3. In order to provide quantitative information about the fraction of different antimony phases during the catalyst activation and FT reaction,

the XANES data were analyzed using fitting with a linear combination of XANES spectra of the reference compounds (Sb_2O_5, Sb_2O_3, antimony foil and $FeSb_2$ antimony-iron alloy). The evolution of the antimony phase composition under the conditions of catalyst activation and catalytic reaction is shown in **Figure 12a** and **b**. The reduction of Sb^{+5} species to Sb^{+3} and then to metallic antimony occurs at relatively low temperatures. Starting from 100°C, metallic Sb species are detected in both the catalysts prepared by impregnation and mechanical mixing. Interestingly, low intensity of the Sb white line after the reduction at 350°C suggests a higher fraction of the antimony metallic phase in the $FeSb/SiO_2$ sample prepared by impregnation, while somewhat lower extent of antimony reduction was observed in the $FeSb/SiO_2$ (m). The XANES fitting is indicative of the presence of FeSb alloy, which appears in both catalysts starting from 150°C (**Figure 12 a** and **b**). As expected, a higher fraction of the FeSb alloy has been detected in the $FeSb/SiO_2$ catalyst prepared by impregnation. Indeed, the STEM -EDX analysis suggests the presence of Fe-Sb core-shell structures (**Figure 4**) in $FeSb/SiO_2$. Important, a noticeable concentration of oxide can be observed in the mechanically mixed $FeSb/SiO_2$ (m) sample (**Figure 12b**), while antimony is only present as the Sb and FeSb metallic species in the catalyst prepared by impregnation after conducting FT reaction (**Figure 12a**). The quality of the analysis of XANES spectra using the linear combination fitting with the reference spectra was estimated from the difference between the experimental spectra and fitting results (**Figure S7a** and **b, SM**). For the activated $FeSb/SiO_2$ and $FeSb/SiO_2$ (m) samples, the difference spectra correspond to 2.0 and 1.6%, respectively.

The XANES data for the catalysts promoted with Sb are consistent with EXAFS results measured for the catalysts cooled down to room temperature in CO after activation and exposure to syngas at 350°C. Interestingly, the EXAFS Fourier transform moduli of the $FeSb/SiO_2$ and $FeSb/SiO_2$ (m) samples are different from that of the antimony foil (**Figure 13 a** and **b**) as they show an additional peak at 2.2 Å. The intensity of this peak is particularly

high in the $FeSb/SiO_2$ catalyst prepared by impregnation. Note that XANES shows almost complete reduction of antimony in the $FeSb/SiO_2$ sample to metallic state. The additional peaks at 2.2 Å seems to be attributable to Sb-Fe coordination in the bimetallic Sb-Fe nanoparticles [43]. The EXAFS results agree with the XANES data (**Figure 12a** and **b**), which are also indicative of a higher fraction of FeSb alloy in the used $FeSb/SiO_2$ catalysts prepared by impregnation and with the STEM-EDX data, showing the Fe-Sb core shell nanoparticles (**Figure 4**).

The situation is different with the tin-promoted catalysts (**Figure 11 c** and **d**). Both calcined $FeSn/SiO_2$ and $FeSn/SO_2$ (m) catalysts contain mostly SnO_2 species with a small fraction of SnO. The intensity of the Sn white line decreases during heating of the tin -promoted catalysts in CO, suggesting gradual tin reduction. The evolution of the tin phase composition in $FeSn/SiO_2$ and $FeSn/SO_2$ (m) calculated from linear decomposition of the catalyst XANES spectra during heating in CO and syngas is shown in **Figure 12 c** and **d**. Note that the tin reduction proceeds much easier for the impregnated catalyst. The tin metallic phase can be already detected at 50-100°C during the exposure of $FeSn/SiO_2$ in CO, while in the $FeSn/SiO_2$ (m) catalyst prepared by mechanical mixing, metallic Sn was observed at much high temperatures (T>175°C) (**Figure 12 d**). Different to the antimony-promoted catalysts, a significant amount of the tin oxide species was still observed after the catalyst activation in CO and exposure to syngas at 350°C. Similar to the antimony-promoted catalysts, the $FeSn/SiO_2$ sample prepared by co-impregnation exhibits a higher fraction of metallic Sn phase and a higher extent of tin reduction, while the $FeSn/SiO_2$ (m) mechanically mixed sample still contains a large fraction of the Sn oxide species (SnO and SnO_2). The estimation of the quality of the analysis of XANES spectra using the linear combination fitting with the reference spectra for calcined $FeSn/SiO_2$ and $FeSn/SiO_2$ (m) (**Figure 8a** and **b, SM**) gives 7.2 % and 3.4% of difference spectra, respectively. For the $FeSn/SiO_2$ and $FeSn/SiO_2$ (m)

catalysts after exposure to syngas, these differences increase to 22.4 and 16.4%, respectively. Higher incertitude of the catalyst analysis after the syngas treatment can be tentatively attributed to the formation of small tin metal nanoparticles or tin carbide species in the presence of CO.

The EXAFS Fourier transform moduli of the calcined tin-promoted $FeSn/SiO_2$ and $FeSn/SiO_2$ (m) catalysts and those after the exposure to syngas at 350°C and cooling down to room temperature in nitrogen are shown in **Figure 13 c** and **d**. The Fourier transform modulus of the tin foil is also shown for comparison. The Fourier transform moduli of the fresh calcined samples display an intense peak at 1.6 Å, which can be attributed to Sn-O coordination. The EXAFS data agree with a large fraction of tin oxide in the calcined iron catalysts promoted with tin, which was also detected by XANES (**Figure 12 c** and **d**). The Fourier transform modulus evolves significantly after the catalyst activation in CO and exposure to the FT reaction. The Fourier transforms of the catalysts activated in CO, exposed to syngas and cooled down to room temperature show (**Figure 13 c** and **d**) the presence of Sn-O coordination shells with a possible small contribution of tin-tin metallic coordination, which was identified by the peak at 2.8 Å. The EXAFS data for the spent catalysts are consistent with XANES, which shows partially reduced tin species in $FeSn/SiO_2$ and $FeSn/SiO_2$ (m) after their activation in CO and reaction. The low intensity of the peaks at 2.8 Å attributed to the Sn-Sn coordination relative to the Sn foil in the promoted iron catalysts suggests the presence of extremely small tin nanoparticles in the used FT catalysts. Indeed, the characterization of the activated $FeSn/SiO_2$ catalysts by STEM (**Figures 3** and **S2, SM**) and XPS showed extremely high tin dispersion. Extremely small Sn nanoparticles were discovered in the activated $FeSn/SiO_2$ by STEM, while XPS showed an increase in the I_{Sn}/I_{Si} ratio in $FeSn/SiO_2$ after the activation in CO (**Table 2**). Note that we did not detect FeSn alloy in the activated and working $FeSn/SiO_2$ catalysts.

Catalytic performance

Carbon monoxide conversion over iron catalysts under the conditions of high temperature FT synthesis results in production of methane, C_2-C_4 olefins, paraffins and higher C_{5+} hydrocarbons. CO_2 and water are also present as reaction products. The catalytic results are summarized in **Figures 14, 15** and **Table 4. Figure 14** displays evolution of carbon monoxide conversion at iso-WHSV (WHSV = 3.6 L g^{-1} h^{-1}) with time on stream over impregnated and mechanically mixed Sn- and Sb- promoted iron catalysts during the first 24 h of reaction. Both non-promoted iron catalysts with 10 and 20 wt. % iron (Fe/SiO_2 and Fe/SiO_2(20%)) showed a gradual decrease in the CO conversion with the reaction time. Note that the iron catalysts promoted with antimony and tin prepared by mechanical mixing exhibit the CO conversion similar to the non-promoted iron catalysts. They also showed gradual deactivation similar to the non-promoted counterparts. The promotion with Sb of the $FeSb/SiO_2$(m) catalyst did not increase FTY, which remained between 0.14-0.26x10^{-4} $mol_{CO}g_{Fe}^{-1}s^{-1}$ with similar selectivities to methane, light olefins and C_{5+} hydrocarbons (**Table 4**). Thus, the catalytic performance and deactivation behavior of the antimony and tin promoted iron catalysts prepared by mechanical mixing is similar to non-promoted iron Fe/SiO_2 catalyst. Fe/SiO_2 (20%) displays a lower FTY (**Table 4**) compared to the Fe/SiO_2 catalyst containing about 10 wt. % Fe. The lower iron-based activity (FTY) of the Fe/SiO_2(20%) can be attributed to larger iron particle size (**Table 1**) and lower concentration of FT active sites.

Note that the $FeSb/SiO_2$ and $FeSn/SiO_2$ catalysts promoted with antimony and tin and prepared by impregnation showed higher FT reaction rate. More specifically, FTY increased 4-5 times after the promotion (**Table 4**). The increase in FTY can be either attributed to better dispersion to the active phase or to the increase in the intrinsic activity of each active site, i.e. increase in the turnover frequency (TOF). The STEM measurements suggest an increase in

the iron particle size in the promoted catalysts activated in CO (**Figure 5**). This suggests somewhat lower iron dispersion in the promoted catalysts. Therefore, the FT rate increase cannot be assigned to the modification of iron dispersion or extent of carbidization but to the increase in TOF (**Table 4**).

The Sb and Sn promoted catalysts, prepared by impregnation reached the stable performance after ~10 h of reaction and did not show any noticeable deactivation during 24 h on stream. Previously, we have shown[22] that this better stability of iron catalyst with the Sn and Sb promoters could be attributed to less significant iron sintering. Note that the most significant promotion phenomena were only observed for the Sb- and Sn-promoted catalyst prepared by impregnation. This suggests that an intimate contact between the promoter and iron active phase is indispensable for attaining higher reaction rate and better stability in FT synthesis. **Figure 15** displays selectivity patterns measured over Fe/SiO_2, $FeSn/SiO_2$, $FeSb/SiO_2$ at iso-conversion (between 10-13%). The promotion results in a slight increase in the methane selectivity (from 24% for Fe/SiO2 catalyst to 28 and 29% for Sb- and Sn- promoted catalysts, respectively) and of a slight increase in the selectivity to light olefins (37 and 35% for Sb- and Sn- promoted catalysts, respectively). These observations are consistent with our previous report [22], which showed only very small variation of light olefin selectivity over silica supported iron catalysts promoted with Sn and Sb. Note that the influence of the promotion with antimony and tin was much more significant on the reaction rate (**Table 4**).

Discussion

The promotion of iron catalysts is an efficient strategy [2] to enhance their performance in the synthesis of light olefins from syngas using Fischer-Tropsch reaction. Our catalytic results show that the FT reaction rate increases 4-5 times after addition of small amounts of antimony or tin to the silica supported iron catalysts. Besides of this major increase in the FT reaction

rate, the promoted iron catalysts exhibit much better stability compared to the non-promoted counterparts (**Table 4**), while the selectivity to light olefins and methane only very slightly increases after the promotion (**Figure 15**). Both metallic antimony and tin have relatively low melting points. It can be considered that under FT reaction conditions, these elements can migrate over the catalyst surface and modify the activity, localization and dispersion of iron species. The diffusion of mobile phase into crystalline lattice will be appreciable at half way to melting point on Kelvin scale. At this temperature, known as Taman temperature, a solid has 70 per cent of its vibrational freedom and its diffusion becomes possible. Metallic antimony and tin have melting points of 631 °C and 232 °C respectively. At the activation and reaction temperature (350 °C), their migration could consequently take place.

However, the migration phenomena seem to be less important compared to the previously studied bismuth and lead catalysts [22,24]. Indeed, the enhancement effects in catalysis were only observed in the $FeSb/SiO_2$ and $FeSn/SiO_2$ catalysts prepared by impregnation, while the catalytic performance and stability of the mechanical mixed catalysts were rather similar to non-promoted Fe/SiO_2 (**Table 4, Figure 14**)

Let us discuss the effect of the promotion with antimony and tin on the characteristics of iron catalysts such as dispersion of active phase and extent of carbidization. There is a general consensus in the literature that the activity of iron catalysis in FT synthesis can be principally attributed to iron carbides, though iron oxides can contribute in a lesser extent by affecting to some extent the intrinsic activity of iron carbide species, enhancing water gas shift and secondary reactions [44–46].

Iron dispersion and extent of iron carbidization are therefore, important parameters, which should be considered in the interpretation of the catalytic data. The characterization performed in this paper suggests, that the promotion with tin and antimony does not result in any positive effect on the iron dispersion. Moreover, the average iron particle size in the activated catalysts

increases from 14.2 in Fe/SiO_2 to 26.7 and 29 nm after the promotion, respectively with tin and antimony (**Figure 5**). Thus, the enhancement of FT reaction rate in the catalysts promoted with antimony and tin cannot be assigned to better iron dispersion.

Let us now evaluate possible contribution of the promoters on iron carbidization. The *in-situ* Mossbauer spectrometry is indicative of better iron carbidization in the presence of the Sb promoter. Almost complete carbidization of iron was observed in $FeSb/SiO_2$ under FT reaction conditions, while some concentrations of the residual iron oxide species were detected in the non-promoted and tin-promoted catalysts (**Table 3**). Higher extent of iron carbidization was observed in the $FeSb/SiO_2$ catalyst prepared by impregnation compared to the $FeSb/SiO_2$ (m) catalyst prepared by mechanical mixing. This suggests that a close interaction between iron and promoter is indispensable for transformation of iron oxide into iron carbide. At the same time, both the Sn-promoted catalysts $FeSn/SiO_2$ and $FeSn/SiO_2$ (m) showed much lower extent of iron carbidization and noticeable concentrations of iron oxide species even under FT reaction conditions. Despite somewhat lower iron carbidization, the FT reaction rate increased several times on the promotion of silica supported iron catalysts with tin (**Table 4**). This suggests that the effect of the tin and antimony promoters on the FT catalytic performance cannot be solely attributed to better iron carbidization.

The catalytic promoters can be of two sorts [7,8]: electronic and structural. The structural promoters improve the dispersion of active phase and catalytic stability, while the electronic promoters influence the intrinsic activity of active sites due to the electronic interactions. More information about the type of the promotion with antimony and tin was extracted from the TOF values. **Table 4** shows the 7-10 times increase in TOF in the iron catalysts promoted with either antimony or tin, while we did not identify any positive influence of antimony and tin on the iron dispersion. No clear effect of Sb and Sn was either uncovered on iron carbidization. Antimony and tin can be therefore considered as electronic promoters, which

mostly affect the intrinsic activity of the iron carbide active sites without noticeable positive effect on iron dispersion and carbidization.

The promoters also improve the stability of silica supported iron nanoparticles in the catalysts prepared by impregnation. Previously, we observed [22] sintering of iron nanoparticles in the non-promoted silica supported catalysts, while the iron carbide particle size remains stable during the FT reaction in the promoted catalysts. The promotion with antimony and tin also increases the stability of iron particle against coke deposition. The TG analysis (**Figure 7**) shows the smaller carbon deposition obtained with the promoted catalysts.

A wide range of characterization techniques employed in this work have provided detailed information about interaction of the active iron phase and promoters. The observed strong effect of the Sb- and Sn-promoters on the catalytic performance of iron catalysts might be therefore due to the intimate contact observed between Fe and the promoter. This contact is more visible in the antimony promoted catalysts. STEM-EDX showed the formation of iron antimony core-shell bimetallic particles in the activated $FeSb/SiO_2$ catalyst (**Figure 4**). *In-situ* XANES showed the presence of Fe-Sb alloy species in the activated and working antimony-promoted iron catalysts under the typical conditions of FT synthesis (**Figure 12a** and **b**). The FeSb alloy was also confirmed by EXAFS. The EXAFS Fourier transform moduli of $FeSb/SiO_2$ and $FeSb/SiO_2$ (m) (**Figure 13a** and **b**) showed the peaks attributed to Sb-Fe coordination in the alloy. As expected, the fraction of the Fe-Sb alloy is less significant in the $FeSb/SiO_2$ (m) catalyst prepared by mechanical mixing. This is consistent with the enhancement of the FT reaction rate observed only for the $FeSb/SiO_2$ catalyst prepared by impregnation (**Table 4**), where the fraction of Fe-Sb bimetallic particles is much higher.

The FT tests also showed a strong promoting effect of tin on the catalytic performance of iron catalysts. Differently to antimony, tin is highly dispersed on silica. In addition, tin cannot be completely reduced to the metallic state as antimony, during the catalyst activation and FT

reaction. *In situ* XANES data showed that more than 30-60% of tin is still in the oxide form after several hours of the FT reaction (**Figure 12c** and **d**). Higher extent of tin reduction was observed in the iron catalyst prepared by impregnation. We did not detect from XANES and EXAFS any distinct Sn-Fe alloy species or alloys. Tin is known to modulate the hydrogenation activity of metal catalysts and is often used as a promoter for a number of selective hydrogenation reactions. Previously, it was shown [47] that the promotion of cobalt catalysts with tin modifies the CO adsorption. Sn preferentially blocks the sites of multiple multi-bonded CO, likely located in hollow sites. The promotion with tin also reduces production of methanol during Fischer-Tropsch synthesis over alumina supported cobalt catalysts [48]. The active sites containing metallic cobalt in interaction with tin oxides favor the selective hydrogenolysis of methyl esters to unsaturated alcohols [49,50].

An interaction of tin with silica support and possible reinsertion of tin cationic species in the silica structure after the catalyst activation in CO was observed by several techniques. XPS, which is a surface sensitive technique, showed a major increase in the I_{Sn}/I_{Si} ratio in $FeSn/SiO_2$ (**Table 2**) after the catalyst activation in CO. In the subsurface layer of silica, tin maintains the Sn^{4+} oxidation state. The XPS data are also consistent with the STEM analysis of the activated $FeSn/SiO_2$ sample. Extremely highly dispersed tin species were discovered (**Figure 3**). Interestingly, STEM also shows higher concentration of tin species in a close proximity to iron carbide nanoparticles (**Figure S2, SM**). This suggests that the mechanism of the promotion of silica supported iron catalysts with tin can be different from that with antimony. The enhancement of FT reaction rate and catalyst stability in the catalyst promoted with antimony can be assigned to the formation of antimony-iron carbide nanoparticles, which were identified using STEM-EDX and XANES/EXAFS. The promotion effect of tin seems to be more relevant to the localization of tin mostly as high dispersed cationic species in the silica and possible very small Sn metallic species in close proximity to the iron carbide

nanoparticles. Both antimony and tin species strongly affect the electronic structure of supported iron carbide nanoparticles. A major increase in the TOF in FT synthesis is observed on the promotion of iron catalysts with these elements. Tentatively, the electronic effect for catalysts promoted by antimony can be explained by the formation of a metallic alloy between Fe-Sb, which modifies the Fermi level. For the catalyst promoted by tin, we did not observe formation of bimetallic particles at the reaction temperature. Indeed, the formation of tin and iron alloy can only start when the temperature exceeds 350 ^{o}C [51]. In this case, the electronic effect could be related to the effect of electron charge transfer and polarization, which can occur, because of localization of mostly tin oxide species in the proximity to iron carbide nanoparticles, which was observed by STEM (**Figure S2, SM**).

Conclusion

The promotion of silica supported iron catalysts with tin and antimony results in a major increase in FT reaction rate. The effect is much more pronounced, when the promoted catalysts were prepared by impregnation compared to the mechanically mixed samples. The promotion with antimony results in some enhancement in iron carbidization, while no visible influence of tin on iron carbidization was observed. Antimony is completely reduced to the metallic state and forms iron-antimony bimetallic nanoparticles under the reaction conditions, while a significant fraction of tin oxide is present in the iron catalysts in FT synthesis. The enhancement of the reaction rate over silica supported iron catalysts promoted with antimony and tin was attributed to the electronic effects arising from the promoters localized in close proximity to the iron carbide nanoparticles. The turnover frequency increases 7-10 times due to the interaction of iron carbide species with antimony and tin.

Acknowledgement

The authors thank Dr Joëlle Thuriot Roukos, Laurence Burylo, Olivier Gardoll and Dr Pardis Simon for the help with elementary analysis, XRD, TPR and XPS measurements. The authors acknowledge financial support from European Union (Interreg V project PSYCHE). GENESIS is supported by the Region Haute-Normandie, the Metropole Rouen Normandie, the CNRS via LABEX EMC and French National Research Agency as a part of the program "Divertissements d'Alene" with the reference ANR-11-EQPX-0020. Part of these experiments was performed at the CLAESS beamline at ALBA Synchrotron. This study was financed in part by the Coordenação de Aperfeiçoamento de Pessoal de Nível Superior – Brasil (CAPES) – Finance Code 001.

Reference

[1] E. de Smit, B.M. Weckhuysen, The renaissance of iron-based Fischer–Tropsch synthesis: on the multifaceted catalyst deactivation behaviour, Chem. Soc. Rev. 37 (2008) 2758. https://doi.org/10.1039/b805427d.

[2] H.M. Torres Galvis, K.P. De Jong, Catalysts for production of lower olefins from synthesis gas: A review, ACS Catal. 3 (2013) 2130–2149. https://doi.org/10.1021/cs4003436.

[3] B.H. Davis, Fischer-Tropsch Synthesis: Reaction mechanisms for iron catalysts, Catal. Today. 141 (2009) 25–33. https://doi.org/10.1016/j.cattod.2008.03.005.

[4] K.M. Brunner, G.E. Harper, K. Keyvanloo, B.F. Woodfield, C.H. Bartholomew, W.C. Hecker, Preparation of an Unsupported Iron Fischer–Tropsch Catalyst by a Simple, Novel, Solvent-Deficient Precipitation (SDP) Method, Energy & Fuels. 29 (2015) 1972–1977. https://doi.org/10.1021/ef5026399.

[5] C.H. Bartholomew, Recent technological developments in Fischer-Tropsch catalysis,

Catal. Letters. 7 (1991) 303–315. https://doi.org/10.1007/BF00764511.

[6] Y. Yang, H. Xiang, R. Zhang, B. Zhong, Y. Li, A highly active and stable Fe-Mn catalyst for slurry Fischer–Tropsch synthesis, Catal. Today. 106 (2005) 170–175. https://doi.org/10.1016/j.cattod.2005.07.127.

[7] G.J. Hutchings, Promotion in heterogeneous catalysis: A topic requiring a new approach?, Catal. Letters. 75 (2001) 1–12. https://doi.org/10.1023/A:1016784122682.

[8] S. Dahl, A. Logadottir, C.J.H. Jacobsen, J.K. Norskov, Electronic factors in catalysis: The volcano curve and the effect of promotion in catalytic ammonia synthesis, Appl. Catal. A Gen. 222 (2001) 19–29. https://doi.org/10.1016/S0926-860X(01)00826-2.

[9] P. Sharma, T. Elder, L.H. Groom, J.J. Spivey, Effect of Structural Promoters on Fe-Based Fischer–Tropsch Synthesis of Biomass Derived Syngas, Top. Catal. 57 (2014) 526–537. https://doi.org/10.1007/s11244-013-0209-9.

[10] D.B. Bukur, D. Mukesh, S.A. Patel, Promoter Effects on Precipitated Iron Catalysts for Fischer-Tropsch Synthesis, Ind. Eng. Chem. Res. 29 (1990) 194–204. https://doi.org/10.1021/ie00098a008.

[11] W. Ngantsoue-Hoc, Y. Zhang, R.J. O'Brien, M. Luo, B.H. Davis, Fischer−Tropsch synthesis: activity and selectivity for Group I alkali promoted iron-based catalysts, Appl. Catal. A Gen. 236 (2002) 77–89. https://doi.org/10.1016/S0926-860X(02)00278-8.

[12] J. Gaube, H.F. Klein, The promoter effect of alkali in Fischer-Tropsch iron and cobalt catalysts, Appl. Catal. A Gen. 350 (2008) 126–132. https://doi.org/10.1016/j.apcata.2008.08.007.

[13] K. Cheng, V. V. Ordomsky, B. Legras, M. Virginie, S. Paul, Y. Wang, A.Y. Khodakov, Sodium-promoted iron catalysts prepared on different supports for high temperature Fischer–Tropsch synthesis, Appl. Catal. A Gen. 502 (2015) 204–214.

https://doi.org/10.1016/j.apcata.2015.06.010.

[14] K. Cheng, V.V. Ordomsky, M. Virginie, B. Legras, P.A. Chernavskii, V.O. Kazak, C. Cordier, S. Paul, Y. Wang, A.Y. Khodakov, Support effects in high temperature Fischer-Tropsch synthesis on iron catalysts, Appl. Catal. A Gen. 488 (2014) 66–77. https://doi.org/10.1016/j.apcata.2014.09.033.

[15] S. Li, A. Li, S. Krishnamoorthy, E. Iglesia, Effects of Zn, Cu, and K promoters on the structure and on the reduction, carburization, and catalytic behavior of iron-based Fischer-Tropsch synthesis catalysts, Catal. Letters. 77 (2001) 197–205. https://doi.org/10.1023/A:1013284217689.

[16] C.-H. Zhang, Y. Yang, B.-T. Teng, T.-Z. Li, H.-Y. Zheng, H.-W. Xiang, Y.-W. Li, Study of an iron-manganese Fischer-Tropsch synthesis catalyst promoted with copper, J. Catal. 237 (2006) 405–415. https://doi.org/10.1016/j.jcat.2005.11.004.

[17] P.A. Chernavskii, V.O. Kazak, G. V. Pankina, Y.D. Perfiliev, T. Li, M. Virginie, A.Y. Khodakov, Influence of copper and potassium on the structure and carbidisation of supported iron catalysts for Fischer–Tropsch synthesis, Catal. Sci. Technol. 7 (2017) 2325–2334. https://doi.org/10.1039/C6CY02676A.

[18] H.M. Torres Galvis, J.H. Bitter, C.B. Khare, M. Ruitenbeek, A.I. Dugulan, K.P. de Jong, Supported Iron Nanoparticles as Catalysts for Sustainable Production of Lower Olefins, Science (80-.). 335 (2012) 835–838. https://doi.org/10.1126/science.1215614.

[19] J. Xie, J. Yang, A.I. Dugulan, A. Holmen, D. Chen, K.P. de Jong, M.J. Louwerse, Size and Promoter Effects in Supported Iron Fischer–Tropsch Catalysts: Insights from Experiment and Theory, ACS Catal. 6 (2016) 3147–3157. https://doi.org/10.1021/acscatal.6b00131.

[20] H.M. Torres Galvis, A.C.J. Koeken, J.H. Bitter, T. Davidian, M. Ruitenbeek, A.I. Dugulan, K.P. de Jong, Effects of sodium and sulfur on catalytic performance of

supported iron catalysts for the Fischer–Tropsch synthesis of lower olefins, J. Catal. 303 (2013) 22–30. https://doi.org/10.1016/j.jcat.2013.03.010.

[21] F. Jiang, M. Zhang, B. Liu, Y. Xu, X. Liu, Insights into the influence of support and potassium or sulfur promoter on iron-based Fischer-Tropsch synthesis: Understanding the control of catalytic activity, selectivity to lower olefins, and catalyst deactivation, Catal. Sci. Technol. 7 (2017) 1245–1265. https://doi.org/10.1039/c7cy00048k.

[22] A.J. Barrios, B. Gu, Y. Luo, D. V. Peron, P.A. Chernavskii, M. Virginie, R. Wojcieszak, J.W. Thybaut, V. V. Ordomsky, A.Y. Khodakov, Identification of efficient promoters and selectivity trends in high temperature Fischer-Tropsch synthesis over supported iron catalysts, Appl. Catal. B Environ. 273 (2020) 119028. https://doi.org/10.1016/j.apcatb.2020.119028.

[23] B. Gu, V. V. Ordomsky, M. Bahri, O. Ersen, P.A. Chernavskii, D. Filimonov, A.Y. Khodakov, Effects of the promotion with bismuth and lead on direct synthesis of light olefins from syngas over carbon nanotube supported iron catalysts, Appl. Catal. B Environ. 234 (2018) 153–166. https://doi.org/10.1016/j.apcatb.2018.04.025.

[24] V. V. Ordomsky, Y. Luo, B. Gu, A. Carvalho, P.A. Chernavskii, K. Cheng, A.Y. Khodakov, Soldering of iron catalysts for direct synthesis of light olefins from syngas under mild reaction conditions, ACS Catal. 7 (2017) 6445–6452. https://doi.org/10.1021/acscatal.7b01307.

[25] B. Gu, S. He, D. V. Peron, D.R. Strossi Pedrolo, S. Moldovan, M.C. Ribeiro, B. Lobato, P.A. Chernavskii, V. V. Ordomsky, A.Y. Khodakov, Synergy of nanoconfinement and promotion in the design of efficient supported iron catalysts for direct olefin synthesis from syngas, J. Catal. 376 (2019) 1–16. https://doi.org/10.1016/j.jcat.2019.06.035.

[26] B. Gu, D. V. Peron, A.J. Barrios, M. Bahri, O. Ersen, M. Vorokhta, B. Šmíd, D.

Banerjee, M. Virginie, E. Marceau, R. Wojcieszak, V. V. Ordomsky, A.Y. Khodakov, Mobility and versatility of the liquid bismuth promoter in the working iron catalysts for light olefin synthesis from syngas, Chem. Sci. 11 (2020) 6167–6182. https://doi.org/10.1039/d0sc01600d.

[27] J.A. Moulijn, A.E. Van Diepen, F. Kapteijn, Catalyst deactivation: Is it predictable? What to do?, Appl. Catal. A Gen. 212 (2001) 3–16. https://doi.org/10.1016/S0926-860X(00)00842-5.

[28] Z. Klencsár, Mössbauer spectrum analysis by Evolution Algorithm, Nucl. Instruments Methods Phys. Res. Sect. B Beam Interact. with Mater. Atoms. 129 (1997) 527–533. https://doi.org/10.1016/S0168-583X(97)00314-5.

[29] T.A. Wezendonk, V.P. Santos, M.A. Nasalevich, Q.S.E. Warringa, A.I. Dugulan, A. Chojecki, A.C.J. Koeken, M. Ruitenbeek, G. Meima, H.U. Islam, G. Sankar, M. Makkee, F. Kapteijn, J. Gascon, Elucidating the Nature of Fe Species during Pyrolysis of the Fe-BTC MOF into Highly Active and Stable Fischer-Tropsch Catalysts, ACS Catal. 6 (2016) 3236–3247. https://doi.org/10.1021/acscatal.6b00426.

[30] Multipurpose in-situ cell (Multi-cell), (n.d.). https://intranet.cells.es/Beamlines/CLAESS/Multi-cell.

[31] B. Ravel, M. Newville, ATHENA, ARTEMIS, HEPHAESTUS: Data analysis for X-ray absorption spectroscopy using IFEFFIT, J. Synchrotron Radiat. 12 (2005) 537–541. https://doi.org/10.1107/S0909049505012719.

[32] H.M. Torres Galvis, J.H. Bitter, T. Davidian, M. Ruitenbeek, A.I. Dugulan, K.P. de Jong, Iron Particle Size Effects for Direct Production of Lower Olefins from Synthesis Gas, J. Am. Chem. Soc. 134 (2012) 16207–16215. https://doi.org/10.1021/ja304958u.

[33] K. Cheng, M. Virginie, V. V. Ordomsky, C. Cordier, P.A. Chernavskii, M.I. Ivantsov, S. Paul, Y. Wang, A.Y. Khodakov, Pore size effects in higherature Fischer-Tropsch

synthesis over supported iron catalysts, J. Catal. 328 (2015) 139–150. https://doi.org/10.1016/j.jcat.2014.12.007.

[34] G. Yu, B. Sun, Y. Pei, S. Xie, S. Yan, M. Qiao, K. Fan, X. Zhang, B. Zong, Fe x O y @C Spheres as an Excellent Catalyst for Fischer−Tropsch Synthesis, J. Am. Chem. Soc. 132 (2010) 935–937. https://doi.org/10.1021/ja906370b.

[35] V. Subramanian, V.V. Ordomsky, B. Legras, K. Cheng, C. Cordier, P.A. Chernavskii, A.Y. Khodakov, Design of iron catalysts supported on carbon-silica composites with enhanced catalytic performance in high-temperature Fischer-Tropsch synthesis, Catal. Sci. Technol. 6 (2016) 4953–4961. https://doi.org/10.1039/c6cy00060f.

[36] M.D. Romero, A. de Lucas, J.A. Calles, A. Rodríguez, Bifunctional catalyst NiHZSM-5: effects of the nickel incorporation method, Appl. Catal. A Gen. 146 (1996) 425–441. https://doi.org/https://doi.org/10.1016/S0926-860X(96)00146-9.

[37] K. Mai, T. Elder, L.H. Groom, J.J. Spivey, Fe-based Fischer Tropsch synthesis of biomass-derived syngas: Effect of synthesis method, Catal. Commun. 65 (2015) 76–80. https://doi.org/10.1016/j.catcom.2015.02.027.

[38] B. Gu, M. Bahri, O. Ersen, A. Khodakov, V.V.V. V. Ordomsky, Self-Regeneration of Cobalt and Nickel Catalysts Promoted with Bismuth for Non-deactivating Performance in Carbon Monoxide Hydrogenation, ACS Catal. 9 (2019) 991–1000. https://doi.org/10.1021/acscatal.8b03991.

[39] J.B. Butt, Carbide phases on iron-based Fischer-Tropsch synthesis catalysts part I: Characterization studies, Catal. Letters. 7 (1991) 61–81. https://doi.org/10.1007/BF00764492.

[40] A.K. Shukla, A.S. Aricò, K.M. El-Khatib, H. Kim, P.L. Antonucci, V. Antonucci, An X-ray photoelectron spectroscopic study on the effect of Ru and Sn additions to platinised carbons, Appl. Surf. Sci. 137 (1999) 20–29. https://doi.org/10.1016/S0169-

4332(98)00483-8.

[41] M.P. Pachamuthu, K. Shanthi, R. Luque, A. Ramanathan, SnTUD-1: a solid acid catalyst for three component coupling reactions at room temperature, Green Chem. 15 (2013) 2158. https://doi.org/10.1039/c3gc40792f.

[42] M. Takaoka, S. Fukutani, T. Yamamoto, M. Horiuchi, N. Satta, N. Takeda, K. Oshita, M. Yoneda, S. Morisawa, T. Tanaka, Determination of chemical form of antimony in contaminated soil around a smelter using X-ray absorption fine structure, Anal. Sci. 21 (2005) 769–773. https://doi.org/10.2116/analsci.21.769.

[43] M. Fehse, D. Bessas, A. Darwiche, A. Mahmoud, G. Rahamim, C. La Fontaine, R.P. Hermann, D. Zitoun, L. Monconduit, L. Stievano, M.T. Sougrati, The Electrochemical Sodiation of FeSb 2 : New Insights from Operando ^{57}Fe Synchrotron Mössbauer and X-Ray Absorption Spectroscopy , Batter. Supercaps. 2 (2019) 66–73. https://doi.org/10.1002/batt.201800075.

[44] S. Li, W. Ding, G.D. Meitzner, E. Iglesia, Spectroscopic and Transient Kinetic Studies of Site Requirements in Iron-Catalyzed Fischer−Tropsch Synthesis, J. Phys. Chem. B. 106 (2002) 85–91. https://doi.org/10.1021/jp0118827.

[45] L.A. Cano, M. V Cagnoli, J.F. Bengoa, A.M. Alvarez, S.G. Marchetti, Effect of the activation atmosphere on the activity of Fe catalysts supported on SBA-15 in the Fischer-Tropsch Synthesis, J. Catal. 278 (2011) 310–320. https://doi.org/10.1016/j.jcat.2010.12.017.

[46] W. Ma, G. Jacobs, D.E. Sparks, J.L.S. Klettlinger, C.H. Yen, B.H. Davis, Fischer–Tropsch synthesis and water gas shift kinetics for a precipitated iron catalyst, Catal. Today. 275 (2016) 49–58. https://doi.org/10.1016/j.cattod.2016.01.006.

[47] A. Paredes-Nunez, D. Lorito, L. Burel, D. Motta-Meira, G. Agostini, N. Guilhaume, Y. Schuurman, F. Meunier, CO Hydrogenation on Cobalt-Based Catalysts: Tin Poisoning

Unravels CO in Hollow Sites as a Main Surface Intermediate, Angew. Chemie - Int. Ed. 57 (2018) 547–550. https://doi.org/10.1002/anie.201710301.

[48] A. Paredes-Nunez, D. Lorito, N. Guilhaume, Y. Schuurman, F.C. Meunier, Effect of Sn on the production of methanol during syngas conversion over Co/alumina, Catal. Today. 336 (2019) 84–89. https://doi.org/10.1016/j.cattod.2019.01.079.

[49] Y. Pouilloux, F. Autin, J. Barrault, Selective hydrogenation of methyl oleate into unsaturated alcohols, Catal. Today. 63 (2000) 87–100. http://www.sciencedirect.com/science/article/pii/S092058610000448X.

[50] K. De Oliveira, Y. Pouilloux, J. Barrault, Selective hydrogenation of methyl oleate into unsaturated alcohols in the presence of cobalt-tin supported over zinc oxide catalysts, J. Catal. 204 (2001) 230–237. https://doi.org/10.1006/jcat.2001.3378.

[51] T.J. Crichton, J.P.G. Farr, The effect of heat treatment on the Fe-Sn alloy system, Trans. Inst. Met. Finish. 82 (2004) 169–173. https://doi.org/10.1080/00202967.2004.11871585.

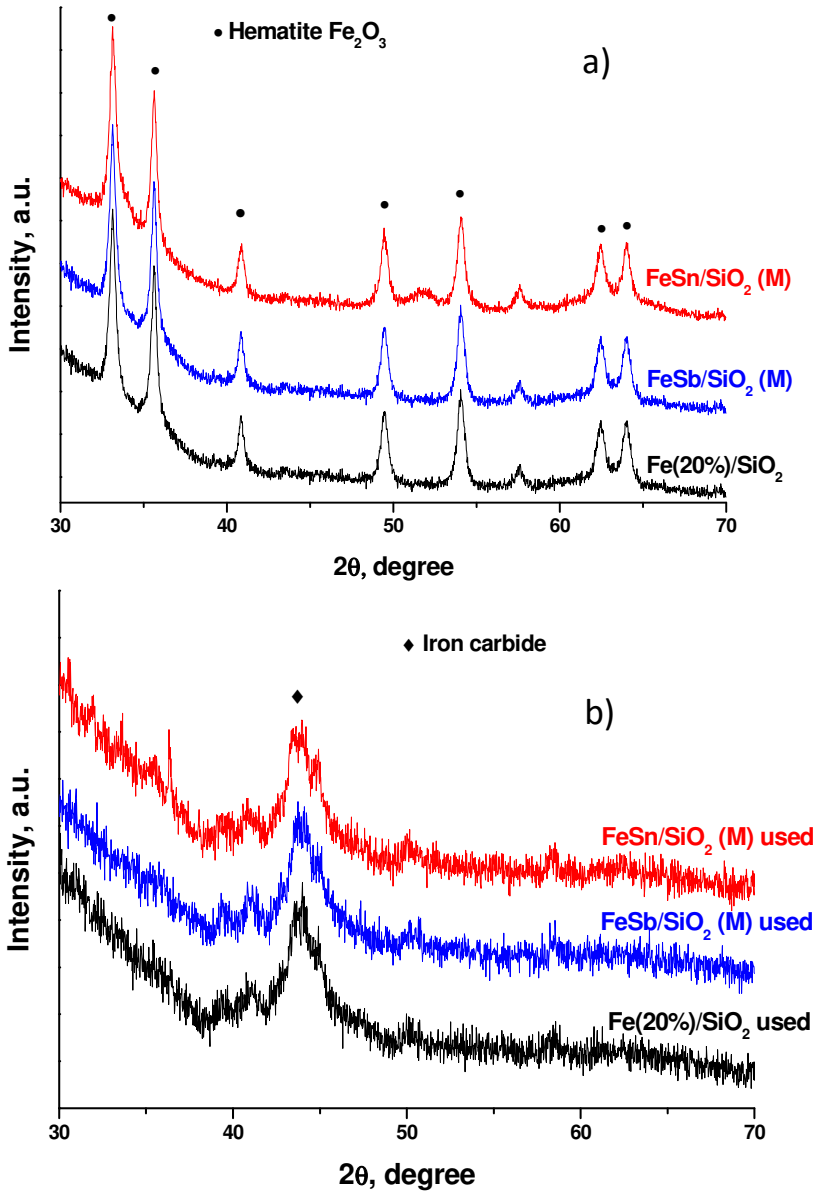

Figure 1. XRD patterns of the catalysts after calcination (a) and after FT reaction (b).

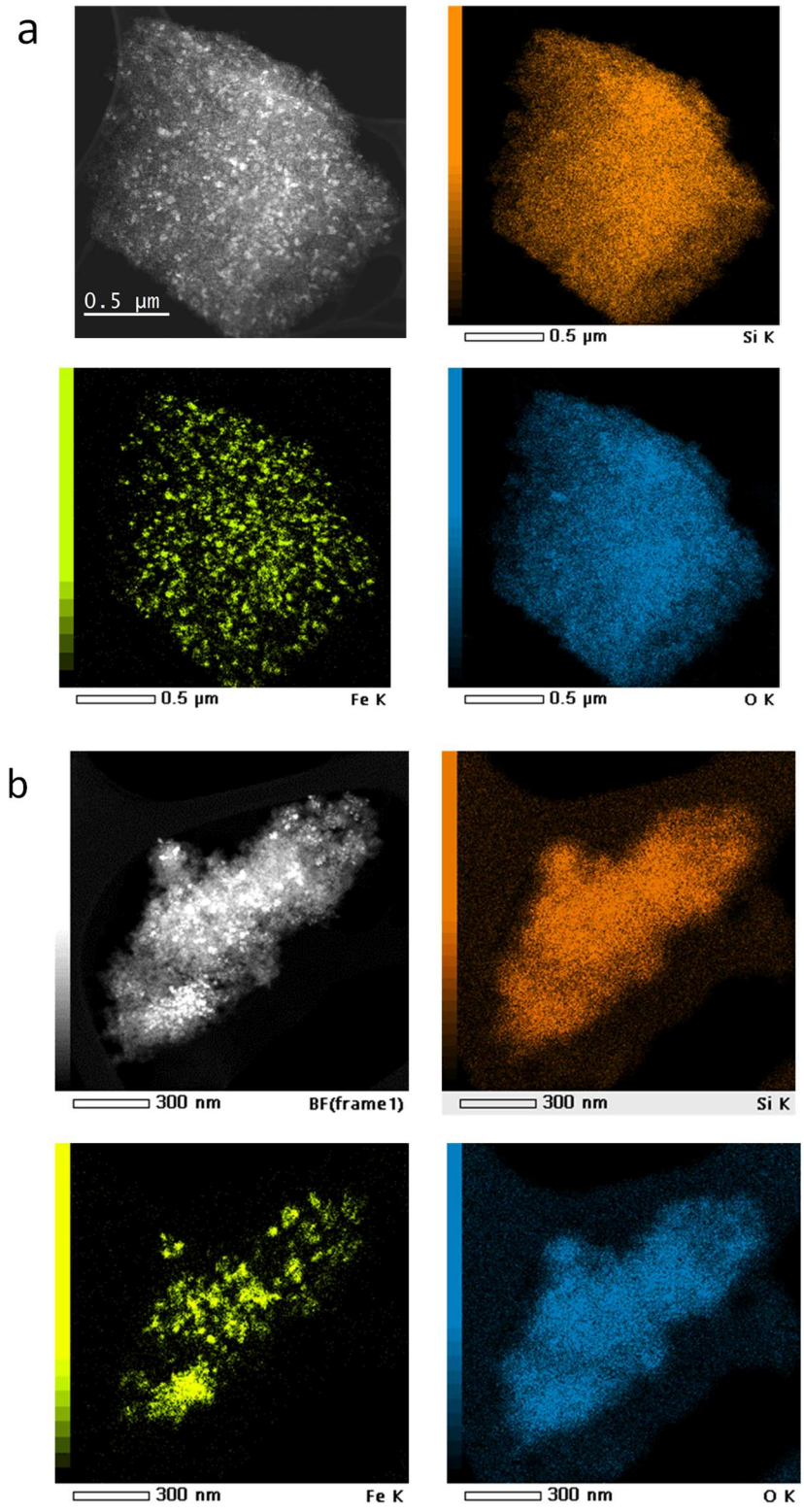

Figure 2. STEM-HAADF and SEM-EDX mapping of the Fe/SiO_2 catalyst: (a) after calcination; (b) after activation in CO.

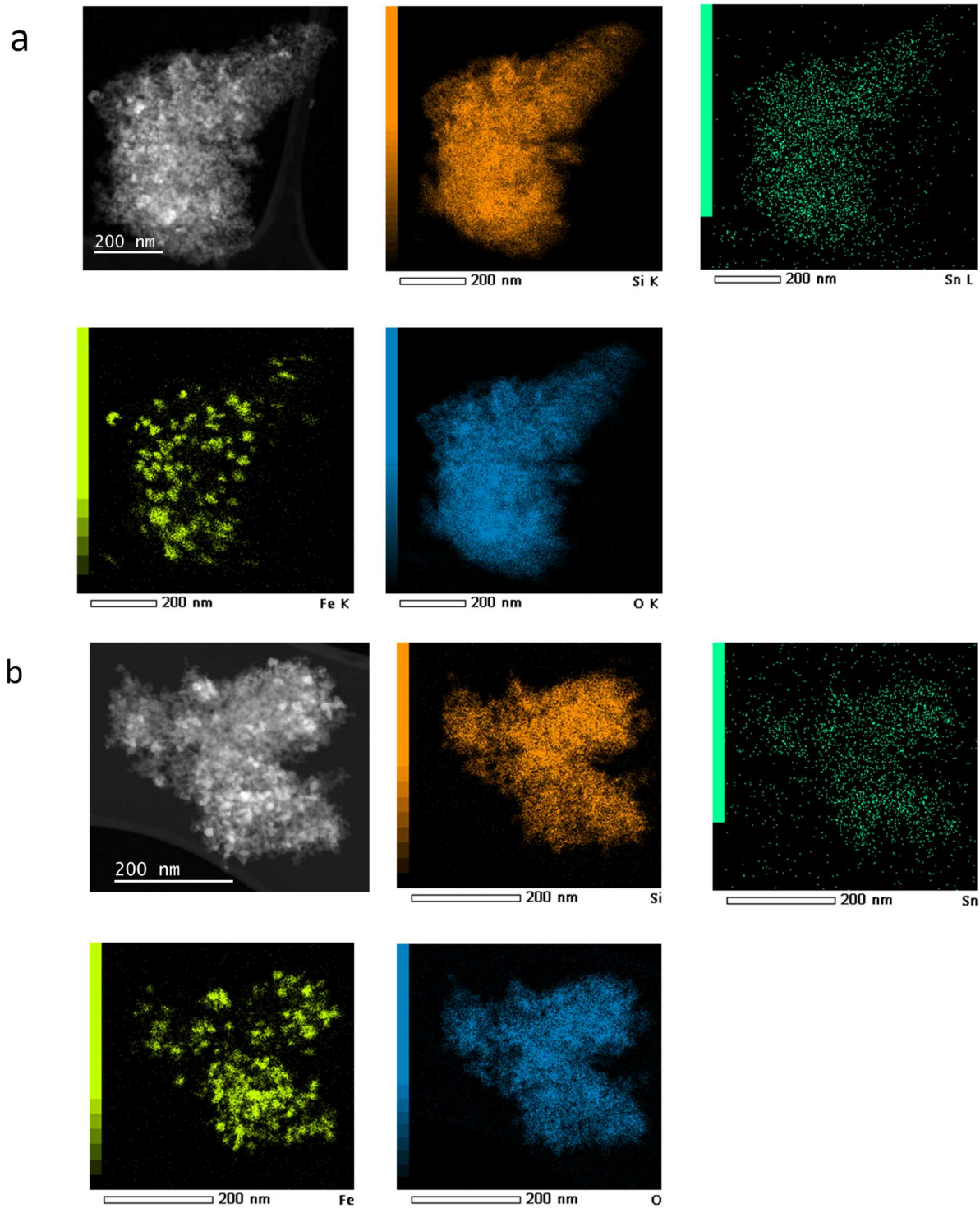

Figure 3. STEM-HAADF and SEM-EDX mapping of the $FeSn/SiO_2$ catalyst: (a) after calcination; (b) after activation in CO.

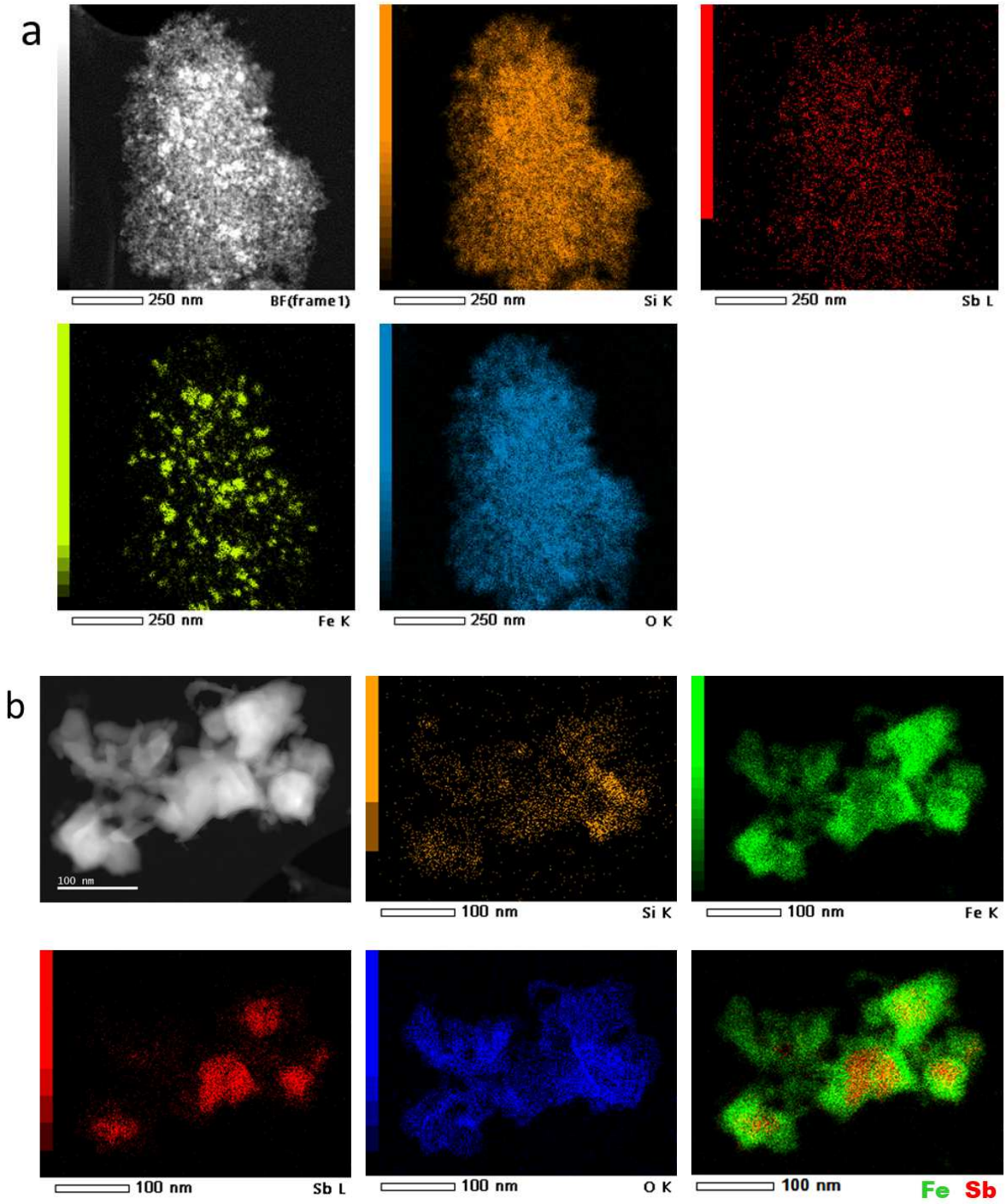

Figure 4. STEM-HAADF and SEM-EDX mapping of the $FeSb/SiO_2$ catalyst: (a) after calcination; (b) after activation in CO showing the formation of Fe-Sb core-shell structures.

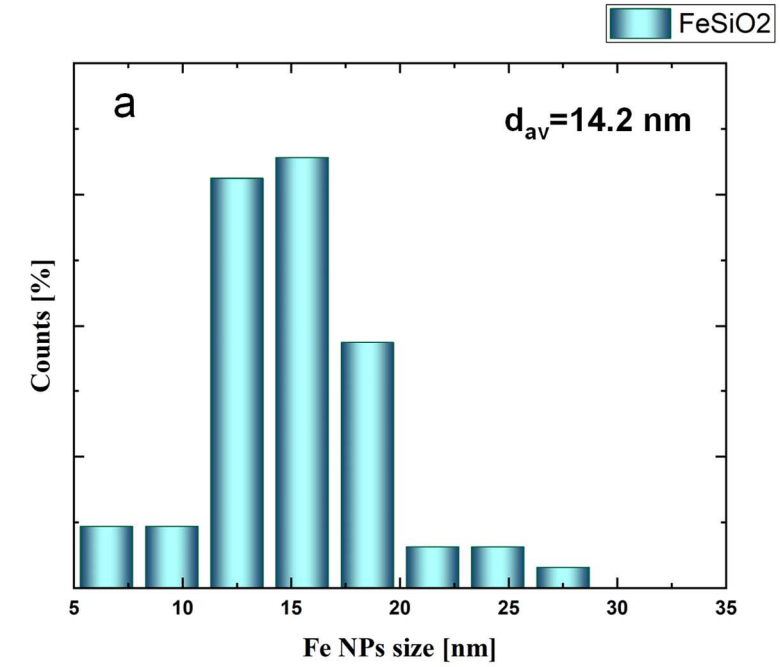
FeSiO2
a
d_{av}=14.2 nm
Counts [%]
5
10
15
20
25
30
35
Fe NPs size [nm]

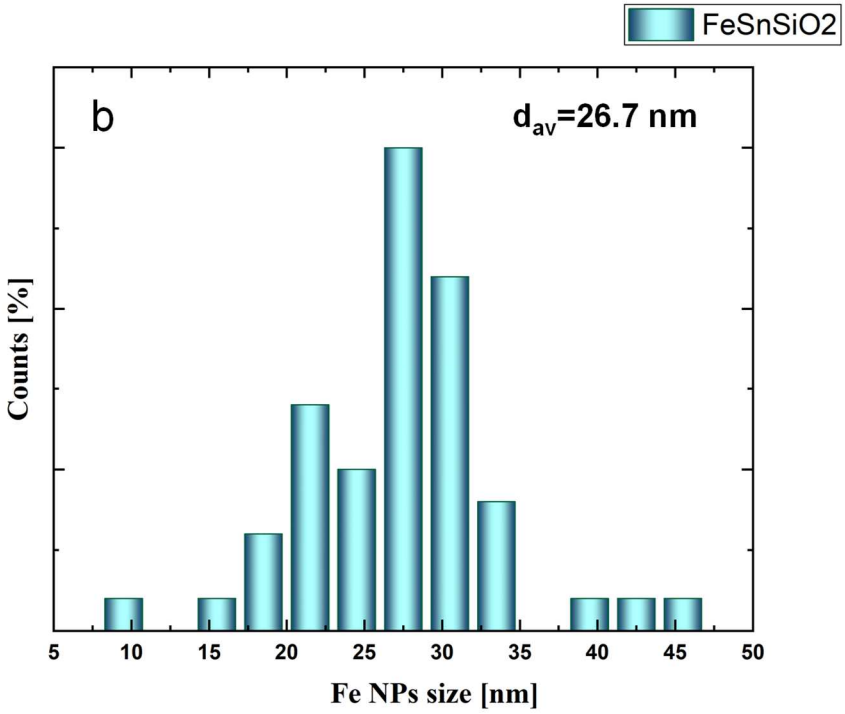
FeSnSiO2
b
d_{av}=26.7 nm
Counts [%]
5
10
15
20
25
30
35
40
45
50
Fe NPs size [nm]

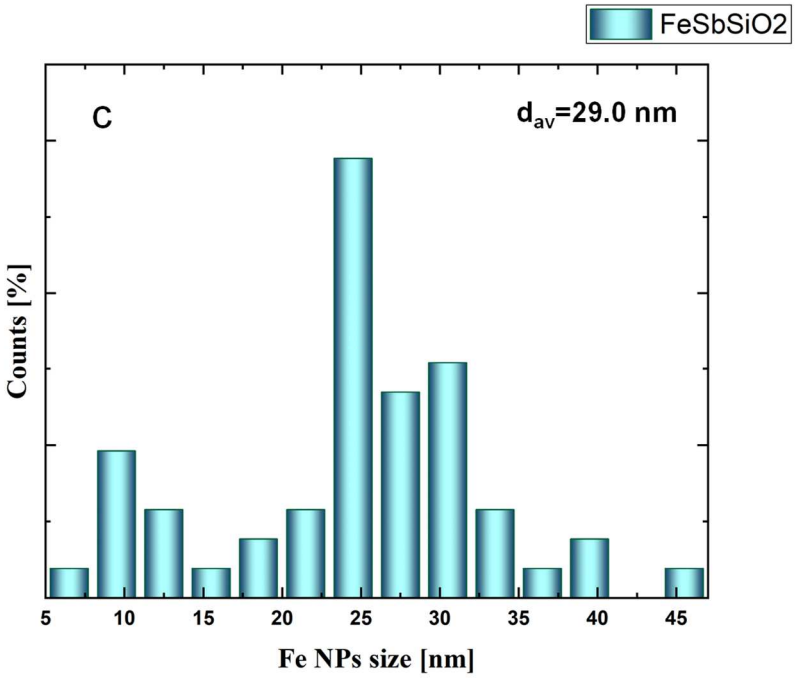

Figure 5. Histograms of iron nanoparticles distribution in silica supported catalysts activated in CO at 350°C: a- Fe/SiO_2, b – $FeSn/SiO_2$, c- $FeSb/SiO_2$.

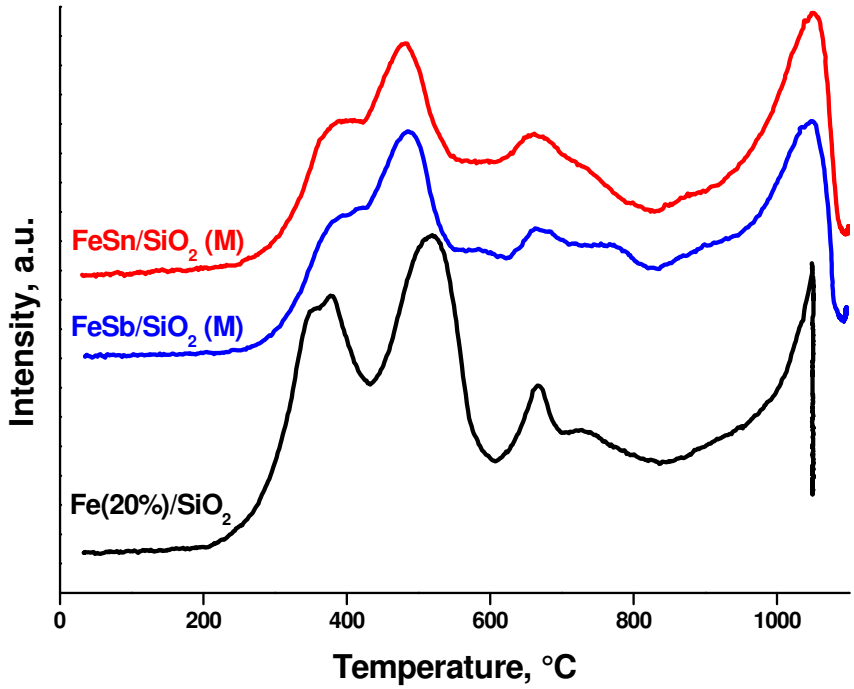

Figure 6. H_2-TPR profiles of Fe(20%)/SiO_2, FeSb/SiO_2 (m) and FeSn/SiO_2 (m) prepared by mechanical mixing.

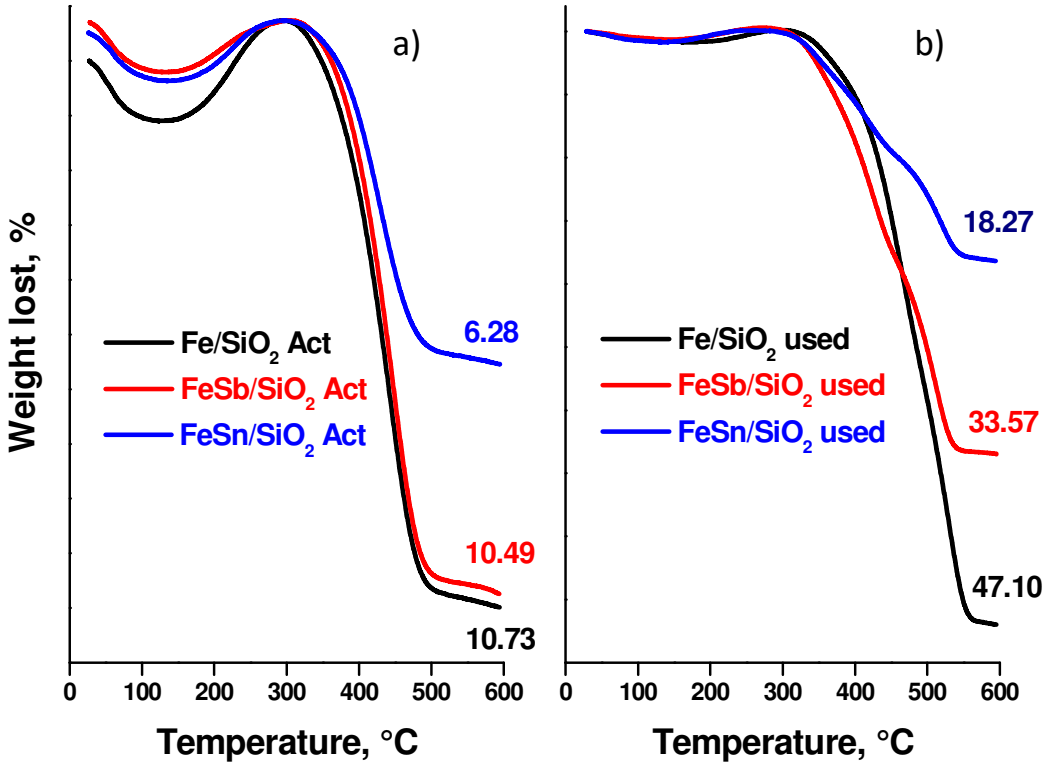

Figure 7. Thermogravimetric analysis (TGA) curves for activated (a) and spent catalysts (b).

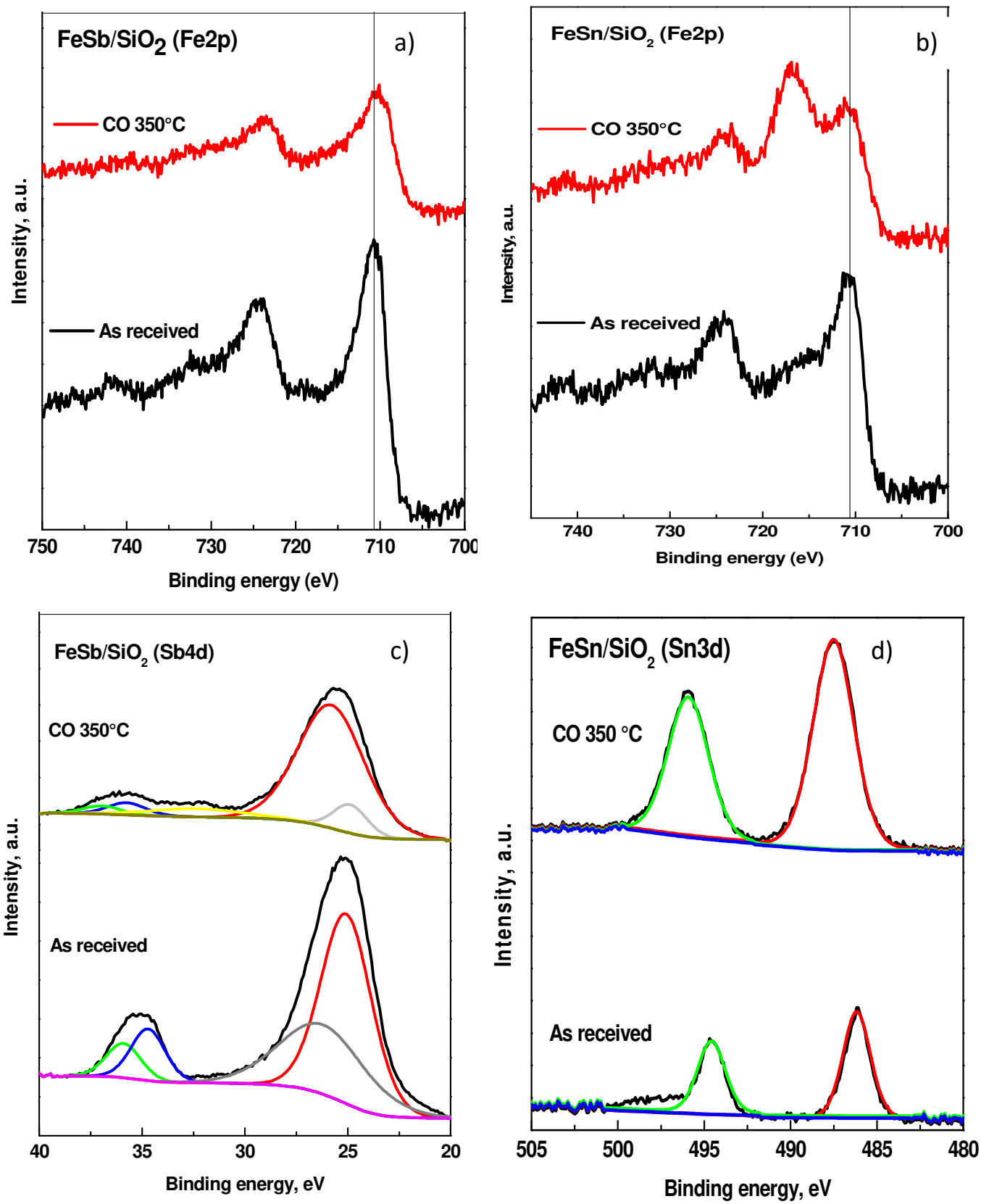

Figure 8. XPS spectra after calcinations and exposure to carbon monoxide: (a) Fe 2p XPS spectra of the $FeSb/SiO_2$ catalyst, (b) Fe 2p XPS spectra of the $FeSn/SiO_2$ catalyst, (c) Sb 4d XPS spectra of the $FeSb/SiO_2$ catalyst, (d) Sn 3d XPS spectra of the $FeSn/SiO_2$catalyst.

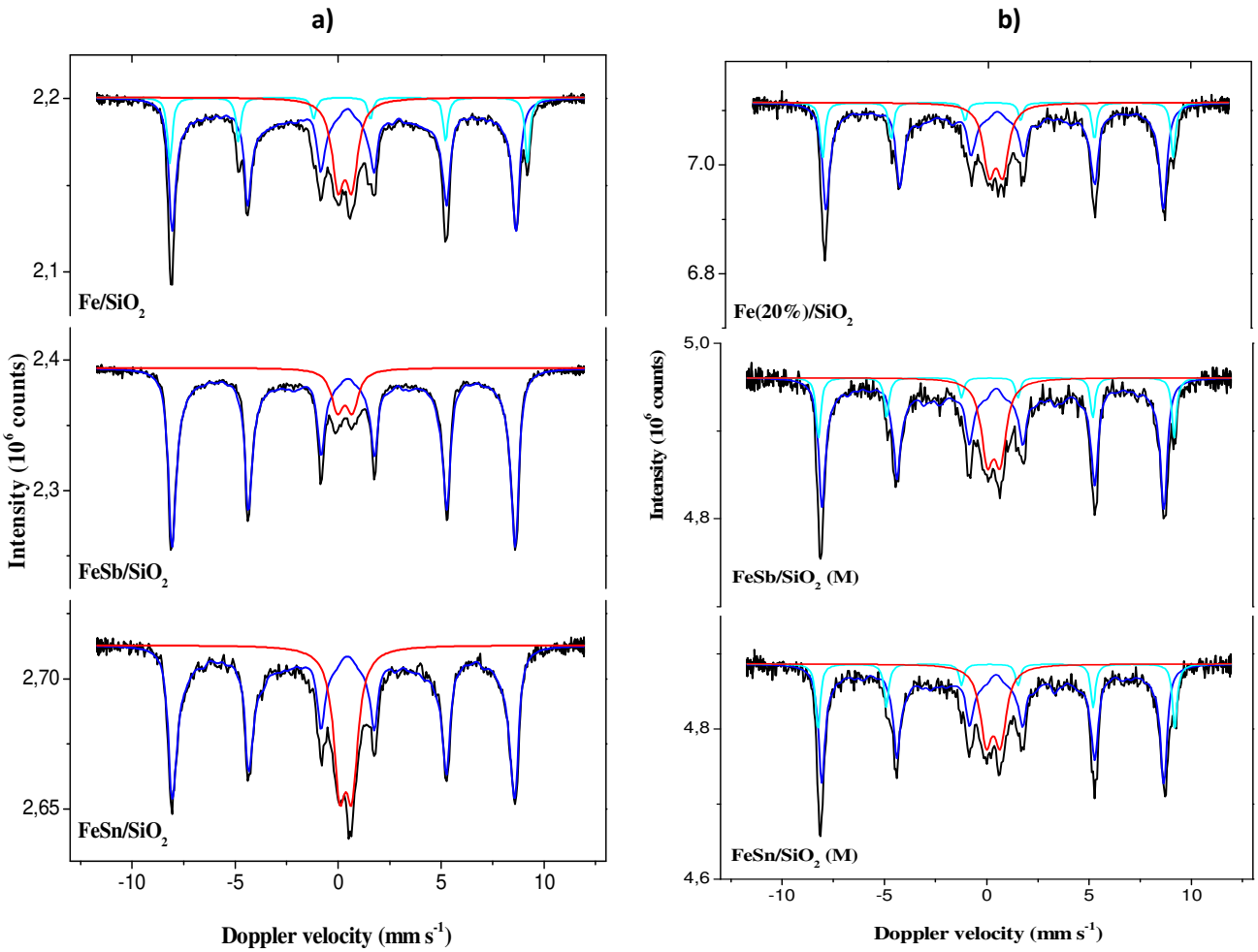

Figure 9. Mössbauer spectra obtained for fresh (a) impregnated and (b) mixed catalysts at -153 °C.

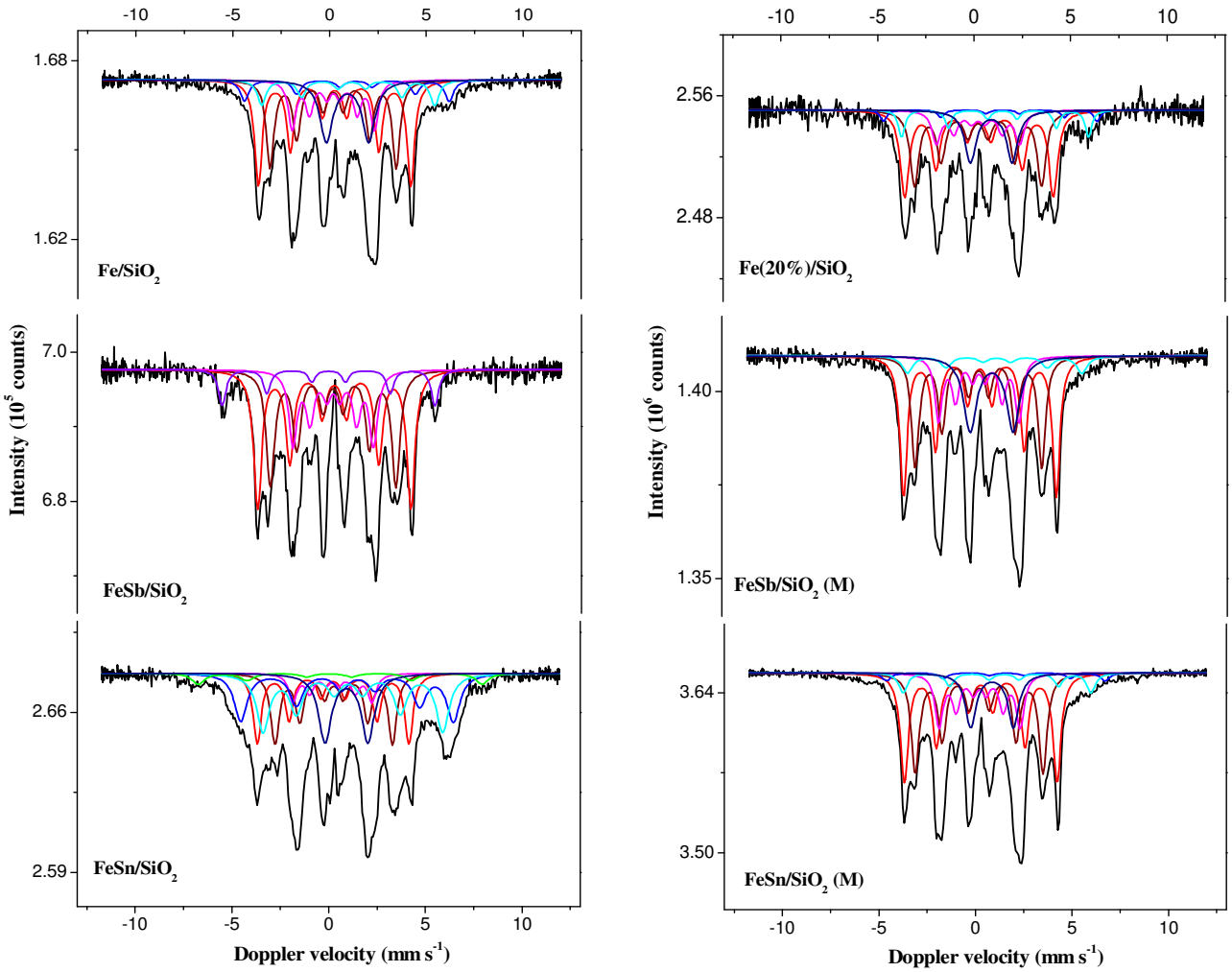

Figure 10. Mössbauer spectra after reaction for impregnated and mixed catalysts at -153 °C.

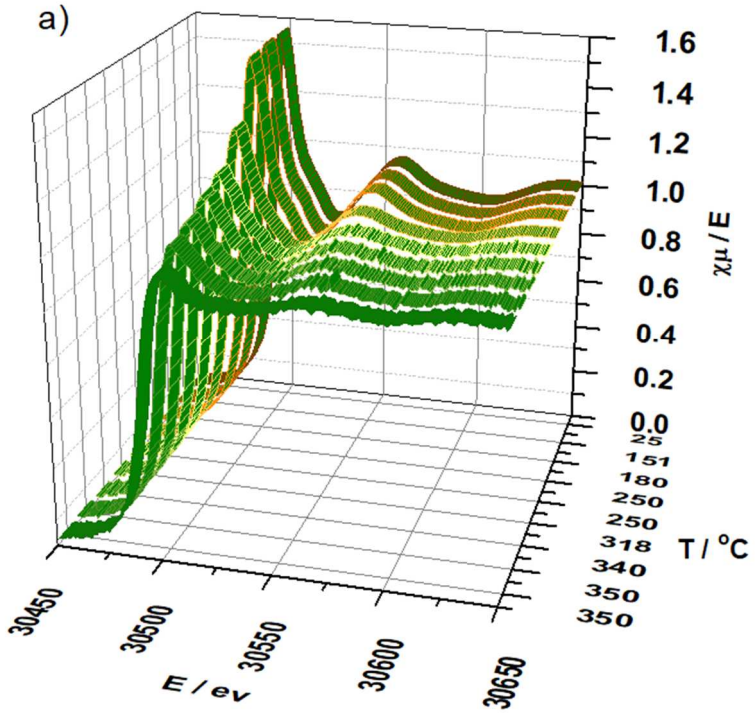
a)
1.6
1.4
1.2
1.0
0.8
0.6
0.4
0.2
0.0
χμ / E
25
151
180
250
250
318
340
350
350
T / °C
30450
30500
30550
30600
30650
E / ev

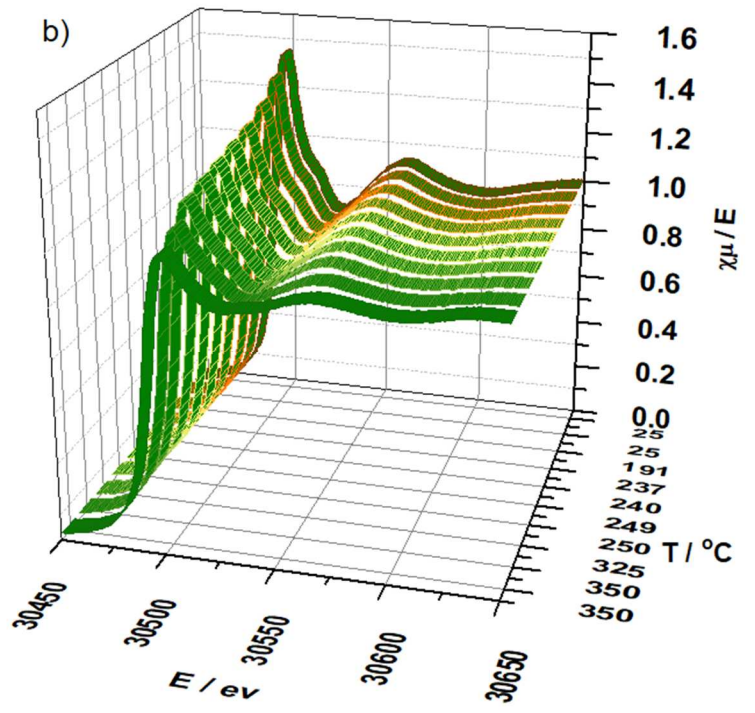
b)
1.6
1.4
1.2
1.0
0.8
0.6
0.4
0.2
0.0
χμ / E
25
25
191
237
240
249
250
325
350
350
T / °C
30450
30500
30550
30600
30650
E / ev

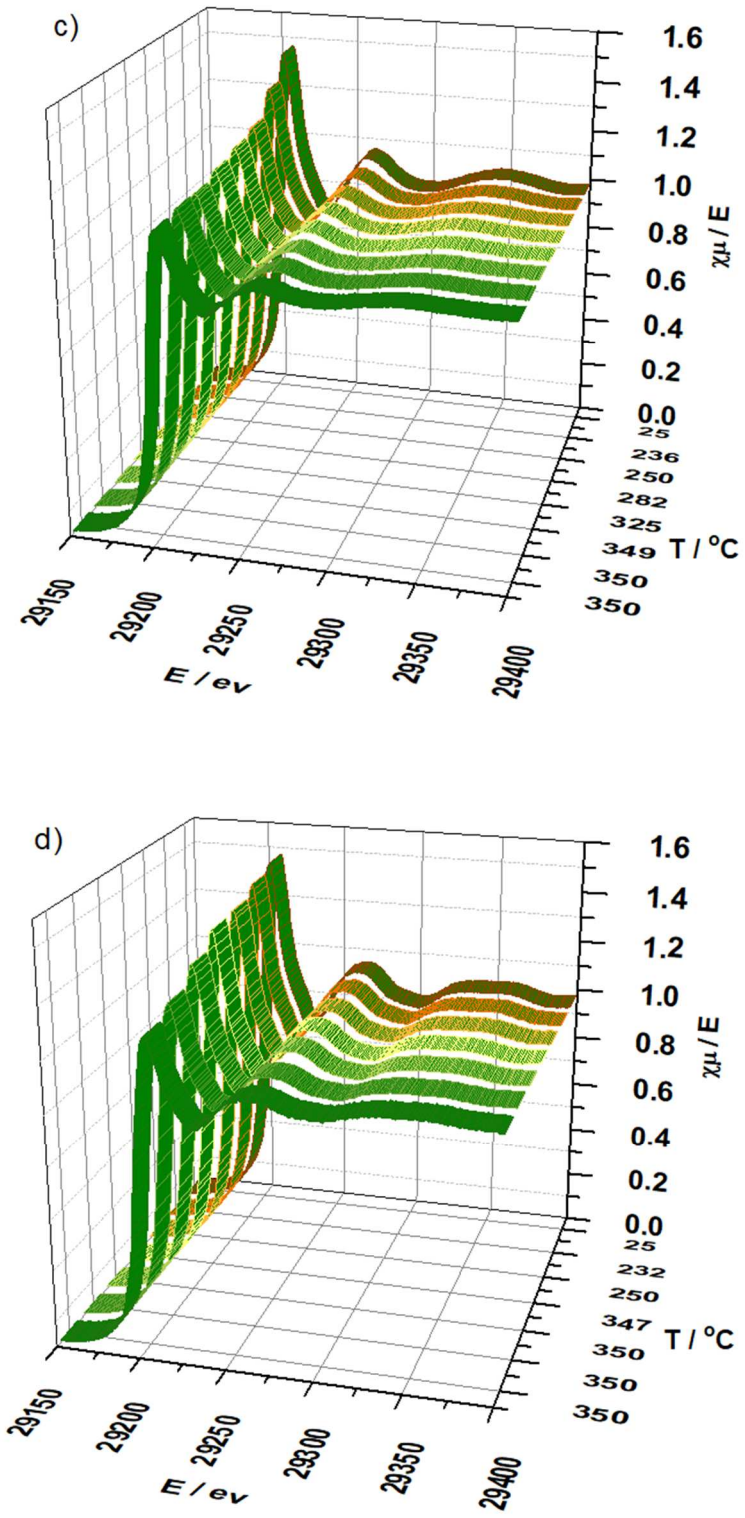

Figure 11. Evolution of the Sb K and Sn absorption edges during the heating in carbon monoxide: a- $FeSb/SiO_2$; b – $FeSb/SiO_2$ (m), c- $FeSn/SiO_2$; d – $FeSn/SiO_2$ (m)

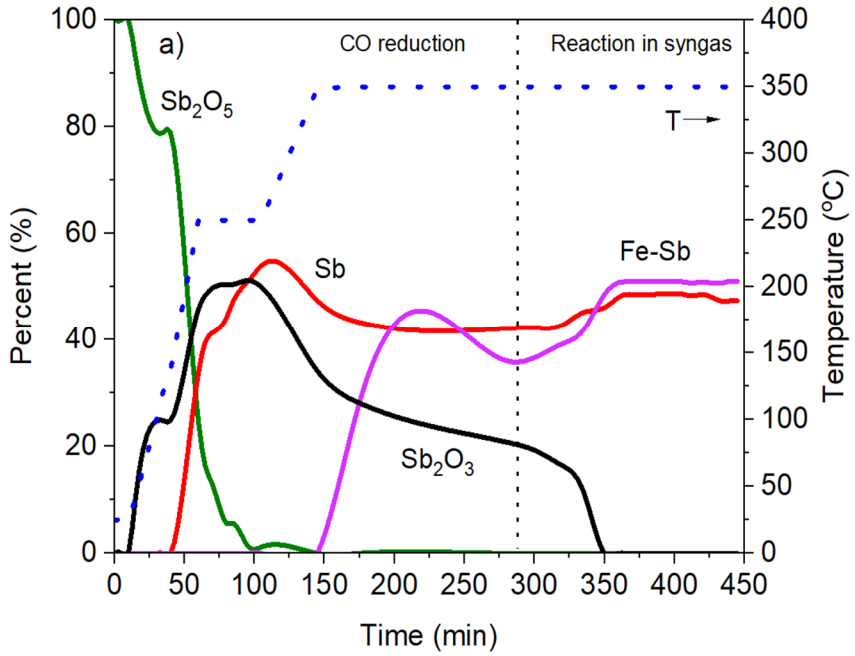
a)
CO reduction
Reaction in syngas
Sb_2O_5
T
Sb
Fe-Sb
Sb_2O_3
Percent (%)
Temperature (°C)
Time (min)
0
20
40
60
80
100
0
50
100
150
200
250
300
350
400
0
50
100
150
200
250
300
350
400
450

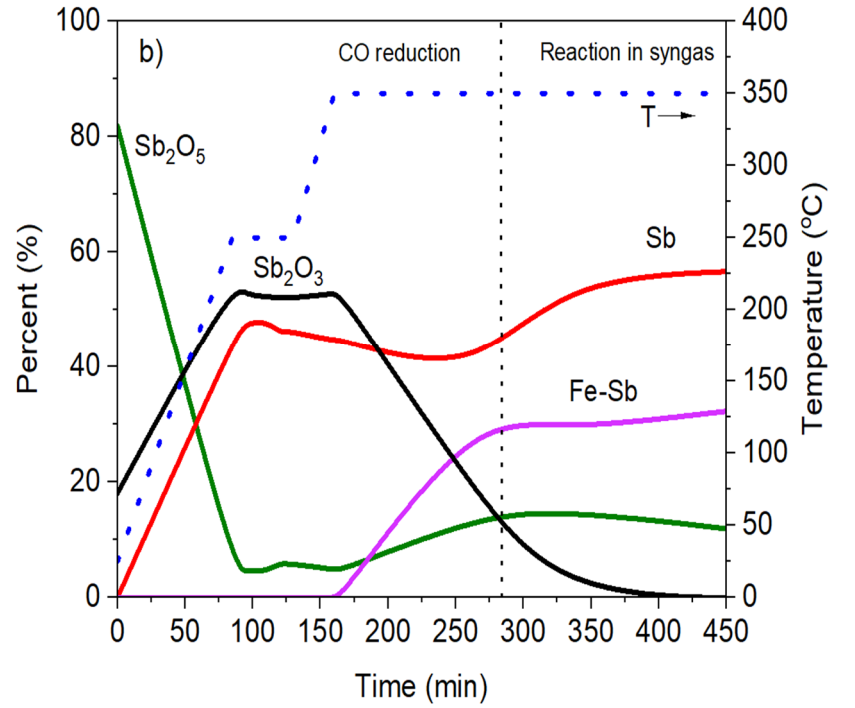
b)
CO reduction
Reaction in syngas
Sb_2O_5
T
Sb
Sb_2O_3
Fe-Sb
Percent (%)
Temperature (°C)
Time (min)
0
20
40
60
80
100
0
50
100
150
200
250
300
350
400
0
50
100
150
200
250
300
350
400
450

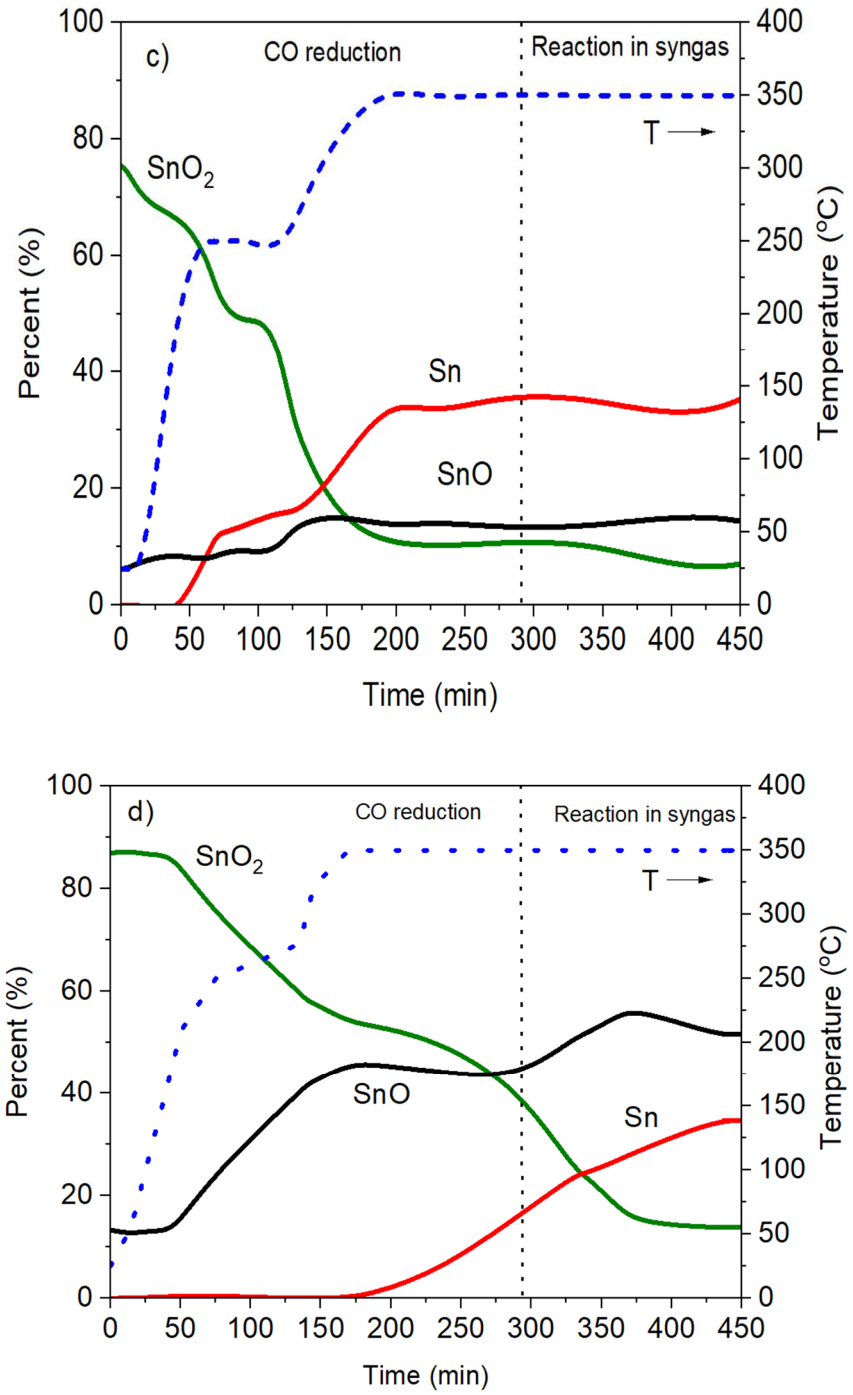

Figure 12. Evolution of the Sb and Sn phase compositions during heating in CO and exposure to syngas at 350°C : a- $FeSb/SiO_2$; b – $FeSb/SiO_2$ (m), c- $FeSn/SiO_2$; d – $FeSn/SiO_2$ (m)

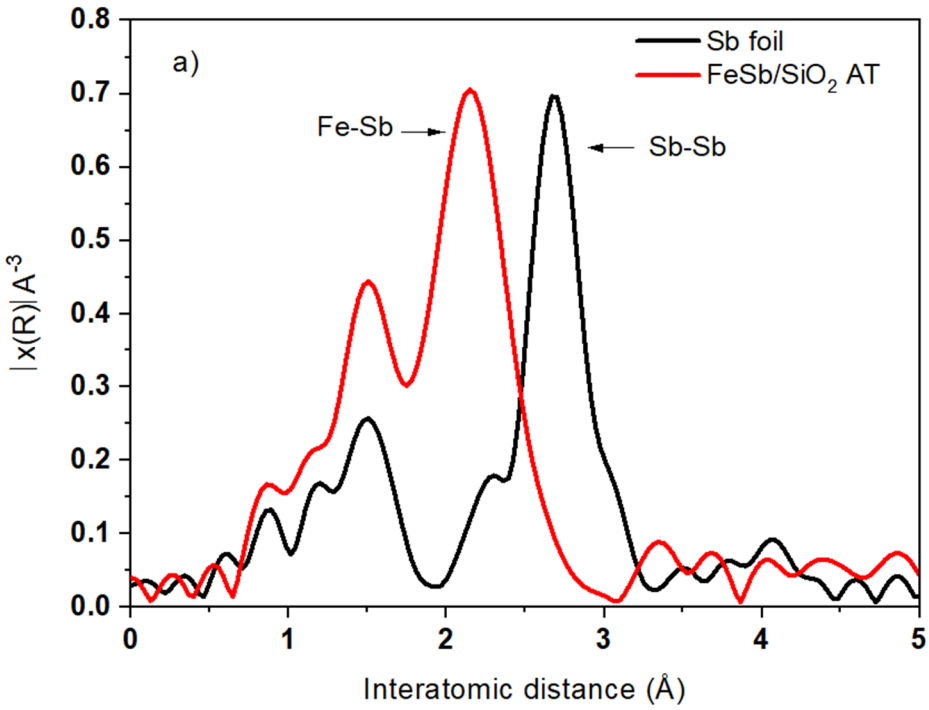
a)
Sb foil
FeSb/SiO2 AT
Fe-Sb
Sb-Sb
|x(R)|A-3
Interatomic distance (Å)

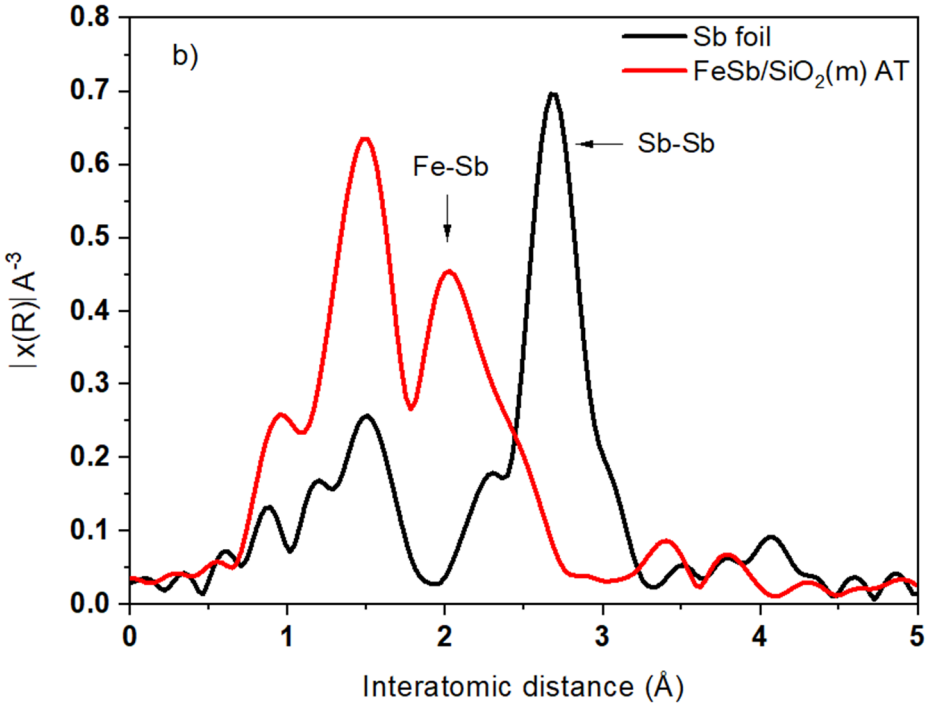
b)
Sb foil
FeSb/SiO2(m) AT
Sb-Sb
Fe-Sb
|x(R)|A-3
Interatomic distance (Å)

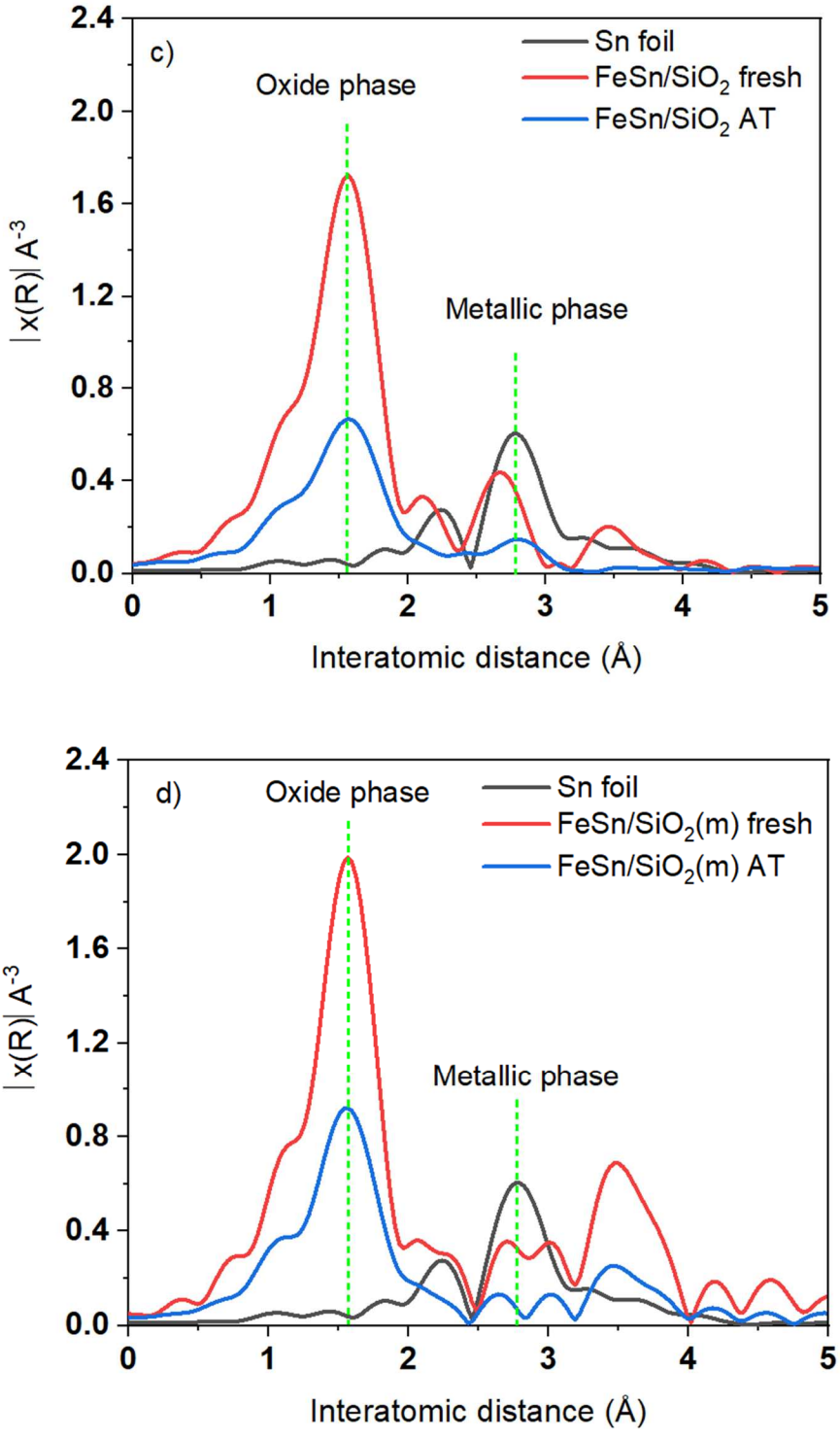

Figure 13. EXAFS Fourier transform moduli of iron catalysts: a - $FeSb/SiO_2$, b - $FeSb/SiO_2$ (m), c - $FeSn/SiO_2$ and d - $FeSn/SiO_2$ (m) after activation in CO, FT reaction and cooling down to ambient temperature.

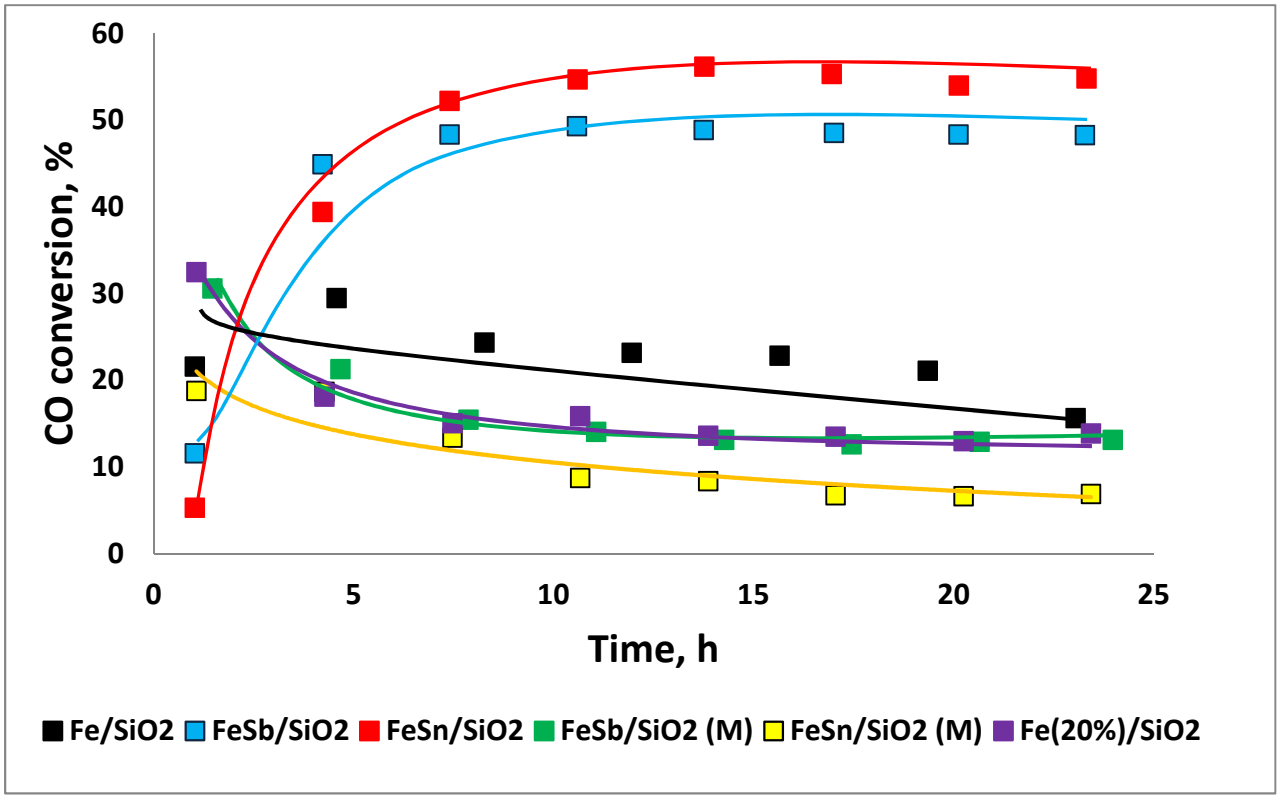

Figure 14. CO conversion as a function of time for iron catalysts promoted with Sn and Sb prepared by co-impregnation and mechanical mixture. Reaction conditions: T = 350 °C, P = 10 bar, H_2/CO = 1, WHSV = 3.6 L g^{-1} h^{-1}.

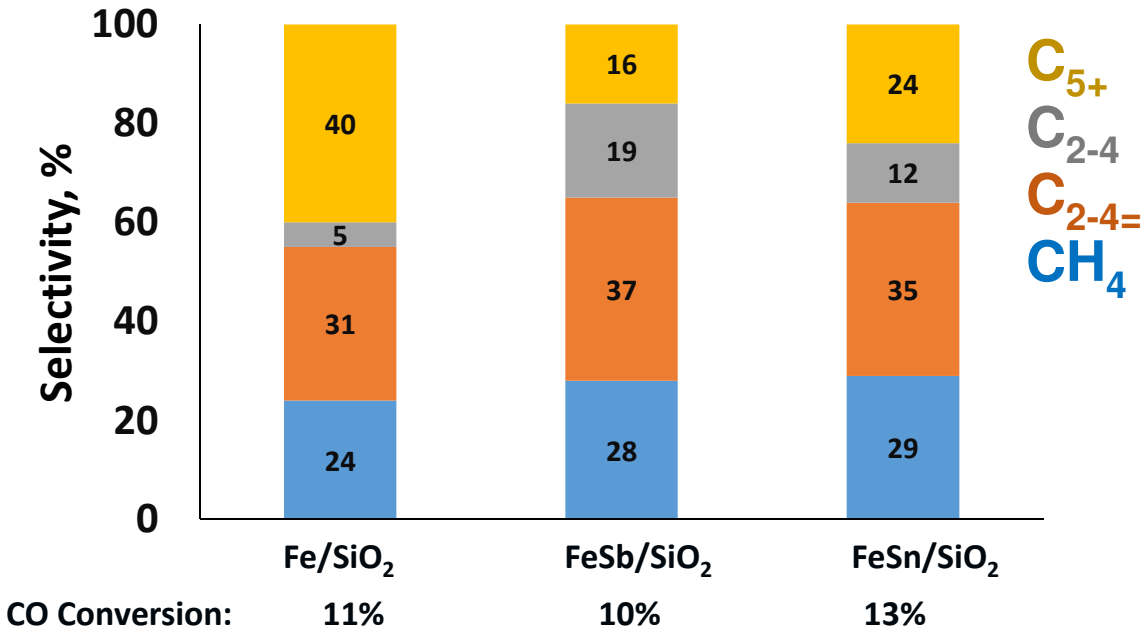

Figure 15. Selectivity patterns over Fe/SiO_2, $FeSb/SiO_2$ and $FeSn/SiO_2$ measured at the CO conversion of 10 - 13 %.

Table 1. Physical properties of supported Fe catalysts.

Sample	Fe content[a] (wt%)	Promoter content[a] (wt%)	D_{oxide}[b] (nm)	Total H_2 consum[c] (mmol/g)	S_{BET}[d] (m^2/g)	V_{tot}[e] (cm^3/g)
Fe/SiO_2	11.2	-	17	2.76	268.5	1.045
$FeSn/SiO_2$	10.9	0.69	11	2.77	263.0	1.041
$FeSb/SiO_2$	9.4	0.72	22	2.70	274.6	1.060
$Fe(20\%)/SiO_2$	21.3	-	21	4.68	203.4	1.021
$FeSn/SiO_2$ (m)	9.2	0.71	20	2.75	229.4	1.035
$FeSb/SiO_2$ (m)	9.2	0.74	21	2.74	228.0	1.032

[a]Fe and promoter content from XRF.

[b]Average particle size of iron oxide by XRD, estimated error 10 %.

[c]The total H_2 consumption and iron reducibility degree from TPR analysis.

[d]BET surface area.

[e]Single point desorption total pore volume of pores, P/P_0=0.975.

Table 2. XPS ration before and after activation

	$FeSb/SiO_2$		**$FeSn/SiO_2$**	
	I_{Fe}/I_{Si}	I_{Sb}/I_{Si}	I_{Fe}/I_{Si}	I_{Sn}/I_{Si}
As received	0.527	0.294	0.402	0.123
After activation in CO 350 °C	0.344	0.264	**-***	0.421

*The value obtained for I_{Fe}/I_{Si} after CO treatment for $FeSn/SiO_2$ is not reliable because of the contribution of Sn peak.

Table 3. The Mössbauer fitted parameters of fresh and spent catalysts, obtained at -153 °C

Sample/ Treatment	*IS* *(mm·s^{-1})*	*QS* *(mm·s^{-1})*	*Hyperfine field (T)*	*Γ* *(mm·s^{-1})*	***Phase***	***Spectral contribution (%)***
Fe/SiO$_2$	0.37	-0.15	51.4*	0.40	α-Fe_2O_3	70
	0.35	0.33	54.0	0.28	α-Fe_2O_3 (Morin[b])	12
	0.33	0.67	-	0.70	Fe^{3+} (SPM)	18
Fe/SiO$_2$ H$_2$/CO=1 350 ℃, 10 bar	0.26	-	24.5	0.47	χ-Fe_5C_2 (I)	30
	0.19	-	20.2	0.47	χ-Fe_5C_2 (II)	26
	0.20	-	13.2	0.47	χ-Fe_5C_2 (III)	14
	1.13	-0.47	32.9	0.54	$Fe_{1-x}O$ (I- Fe^{2+})	7
	1.06	-0.18	27.8	0.54	$Fe_{1-x}O$ (II- Fe^{2+})	8
	0.93	2.19	-	0.79	$Fe_{1-x}O$ (SPM)	15
Fe(20)/SiO$_2$ Fresh sample	0.37	-0.15	51.8*	0.43	α-Fe_2O_3	69
	0.32	0.32	53.9	0.28	α-Fe_2O_3 (Morin)	13
	0.35	0.67	-	0.70	Fe^{3+} (SPM)	18
Fe(20)/SiO$_2$ H$_2$/CO=1 350 ℃, 10 bar	0.26	-	23.9	0.54	χ-Fe_5C_2 (I)	33
	0.20	-	20.5	0.54	χ-Fe_5C_2 (II)	29
	0.19	-	13.4	0.54	χ-Fe_5C_2 (III)	14
	1.16	-0.65	34.4	0.40	$Fe_{1-x}O$ (I- Fe^{2+})	3
	1.27	-0.37	30.1	0.40	$Fe_{1-x}O$ (II- Fe^{2+})	8
	0.89	2.16	-	0.70	$Fe_{1-x}O$ (SPM)	13
FeSb/SiO$_2$	0.36	-0.20	51.5*	0.40	α-Fe_2O_3	89
	0.33	0.73	-	0.70	Fe^{3+} (SPM)	11
FeSb/SiO$_2$ H$_2$/CO=1 350 ℃, 10 bar	0.26	-	24.6	0.51	χ-Fe_5C_2 (I)	38
	0.20	-	20.1	0.51	χ-Fe_5C_2 (II)	32
	0.21	-	12.9	0.51	χ-Fe_5C_2 (III)	21
	0.00	-	34.1	0.45	Fe^0	9
FeSn/SiO$_2$	0.36	-0.20	51.3*	0.40	α-Fe_2O_3	74
	0.37	0.60	-	0.70	Fe^{3+} (SPM)	26
FeSn/SiO$_2$ H$_2$/CO=1 350 ℃, 10 bar	0.27	-	24.3	0.51	χ-Fe_5C_2 (I)	18
	0.24	-	19.0	0.51	χ-Fe_5C_2 (II)	17
	0.20	-	12.7	0.51	χ-Fe_5C_2 (III)	8
	0.31	0.36	45.7	0.80	$Fe_{1-x}O$ (I- Fe^{3+})	4
	1.24	-0.57	34.2	0.80	$Fe_{1-x}O$ (II- Fe^{2+})	18
	1.14	-0.14	29.7	0.80	$Fe_{1-x}O$ (III- Fe^{2+})	22
	0.93	2.22	-	0.80	$Fe_{1-x}O$ (SPM)	13
FeSb/SiO$_2$ (M)	0.37	-0.15	51.8*	0.40	α-Fe_2O_3	70
	0.32	0.33	54.0	0.28	α-Fe_2O_3 (Morin)	12
	0.34	0.64	-	0.70	Fe^{3+} (SPM)	18
FeSb/SiO$_2$ (M) H$_2$/CO=1 350 ℃, 10 bar	0.27	-	24.4	0.45	χ-Fe_5C_2 (I)	34
	0.21	-	20.2	0.45	χ-Fe_5C_2 (II)	28
	0.22	-	12.9	0.45	χ-Fe_5C_2 (III)	16
	1.08	-0.10	27.9	0.67	$Fe_{1-x}O$ (Fe^{2+})	6
	0.88	2.21	-	0.81	$Fe_{1-x}O$ (SPM)	16
FeSn/SiO$_2$ (M)	0.37	-0.16	51.8*	0.40	α-Fe_2O_3	69
	0.32	0.33	54.1	0.28	α-Fe_2O_3 (Morin)	13
	0.33	0.69	-	0.70	Fe^{3+} (SPM)	18
FeSn/SiO$_2$ (M) H$_2$/CO=1 350 ℃, 10 bar	0.27	-	24.6	0.49	χ-Fe_5C_2 (I)	33
	0.20	-	20.5	0.49	χ-Fe_5C_2 (II)	31
	0.22	-	13.0	0.49	χ-Fe_5C_2 (III)	16
	1.34	-0.57	35.2	0.54	$Fe_{1-x}O$ (I- Fe^{2+})	3
	1.30	-0.36	30.3	0.54	$Fe_{1-x}O$ (II- Fe^{2+})	6
	0.86	2.21	-	0.68	$Fe_{1-x}O$ (SPM[a])	11

Table 4. Catalytic performance of iron catalysts promoted with Sn and Sb in FT synthesis measured in a conventional fixed bed reactor at iso-WHSV (10 bar, 350 °C, H_2/CO = 1/1, WHSV = 3.6 L/g.h, TOS = 24h)

Catalysts	FTY 10^{-4} $mol_{CO}g_{Fe}^{-1}s^{-1}$	TOF[a], s^{-1}	CO conv. (%)	CO_2 select. (%)	Hydrocarbon selectivity (%)				$C_{2-4}^{=}/C_{2-4}^{o}$
					CH_4	$C_{2-4}^{=}$	C_{2-4}^{0}	C_5^+	
Fe/SiO_2	0.20	0.090	11	15	24	31	5	40	6.20
$FeSn/SiO_2$	0.98	0.840	53	49	23	17	13	47	1.31
$FeSb/SiO_2$	0.87	0.690	47	47	14	17	10	59	1.70
$Fe(20\%)/SiO_2$	0.13	-	14	47	24	34	6	36	5.67
$FeSn/SiO_2$ (m)	0.14	-	8	26	28	33	6	33	5.50
$FeSb/SiO_2$ (m)	0.26	-	14	24	18	24	5	53	4.8

[a]TOF calculated using the average iron carbide particle size from TEM for the activated catalysts

Graphical abstract